Ultrasonics - Sonochemistry 51 (2019) 424–438

Contents lists available at ScienceDirect

Ultrasonics - Sonochemistry

journal homepage: www.elsevier.com/locate/ultson

Cross-frequency couplings in non-sinusoidal dynamics of interacting oscillators: Acoustic estimation of the radial position and spatial stability of nonlinear oscillating bubbles

Damián Dellavale[a,*], Juan Manuel Rosselló[b]

[a] Departamento de Física Médica – Laboratorio de Bajas Temperaturas, Instituto Balseiro – CONICET, Centro Atómico Bariloche (R8402AGP), Río Negro, Argentina
[b] Laboratorio de Cavitación y Biotecnología, Instituto Balseiro – CONICET, Centro Atómico Bariloche (R8402AGP), Río Negro, Argentina

ARTICLE INFO

Keywords:
Cross-frequency coupling
Phase locking value
Multi-frequency bubble driving
Active acoustic-field manipulation
Sonoluminescence

ABSTRACT

In this work, the analysis of cross-frequency couplings (CFC) is introduced in the context of nonlinear acoustics related to the dynamics of bubble(s)-resonator systems. The results obtained from experiments specifically designed to untangle the causal connection between the CFC patterns observed at the signal level and the underlying physical processes, are discussed. It was found that "causal" amplitude-to-amplitude (AAC) and amplitude-to-phase (APC) couplings emerge in the system dynamics as a consequence of the bubble(s)-resonator mechanistic interaction in the oscillatory steady-state. In these CFC patterns, the amplitude of the fundamental frequency component (f_0) effectively modulates the amplitude and relative phase of the harmonic components (Nf_0). Moreover, these AAC and APC couplings give rise to "epiphenomenal" phase-to-amplitude (PAC) and phase-to-phase (PPC) couplings, in which the link between modulating and modulated parameters represents a correlation rather than a causal connection. It is shown that these CFC patterns can be exploited to determine the presence, spatial stability and radial position of nonlinear oscillating bubble(s) trapped within the acoustic chamber. Potential applications of the proposed techniques are also discussed. Substantial evidence is presented showing that CFC patterns emerging from quasi-periodic non-sinusoidal waveforms are informative on the interaction between underlying oscillators.

1. Introduction

The phenomenon of nonlinear oscillating bubbles trapped in a standing sound wave developed within an acoustic chamber can be thought as a system of coupled oscillators (i.e. the bubble(s) and the normal modes of the acoustic resonator). This scenario is commonly found in sonoluminescence, sonochemistry and acoustic cavitation experiments. In a typical experimental setup, the acoustic chamber is forced to oscillate in one of its normal modes by means of external piezoelectric drivers. If the driving amplitude is high enough, the chamber oscillatory dynamics becomes nonlinear leading to the possibility of modal interactions via internal resonances [1]. On the other hand, the radial dynamics of the bubble ($R(t)$) is described by the Rayleigh-Plesset-Keller equation generalized for non-equilibrium condensation-evaporation mass transfer at the bubble interface [2]. In particular, when the amplitude of the acoustic pressure field is slightly above the static pressure of the fluid, the bubble oscillatory regime becomes highly nonlinear giving rise to the sonoluminescence (SL) phenomenon. Under this situation, the energy focused in the spherically inertial collapses is enough to produce a sudden rise in the pressure, density and gas temperature within the bubble. Consequently, a hot plasma core is generated from the gas and a very short (100 ps–2 ns) pulse of light is emitted (from infrared to ultraviolet) [3].

As a consequence of the highly nonlinear dynamics discussed above, sub-harmonics and harmonics of the fundamental driving frequency are commonly observed in the spectral signature of bubble(s)-resonator systems [4,5]. Recently, we reported preliminary evidence suggesting that nonlinear interaction between different frequency bands in the form of cross-frequency coupling (CFC) takes place in bubble(s)-resonator systems [1]. From the signal processing point of view, CFC refers to the correlation between the phase/amplitude of a low-frequency band with those of a high-frequency band within or across time series. The nonlinear interaction between different frequencies in the form of CFC is a rather ubiquitous phenomenon that has been observed in a variety of physical systems: earth seismic waves, stock market fluctuations, pulsatile hormone secretions and in the electrical activity

* Corresponding author.
E-mail address: dellavale@cab.cnea.gov.ar (D. Dellavale).

https://doi.org/10.1016/j.ultsonch.2018.07.026
Received 17 February 2018; Received in revised form 5 July 2018; Accepted 19 July 2018
Available online 21 July 2018
1350-4177/

of the human brain (see Refs. [6,7] and references therein). In particular, the CFC phenomenon has received special attention in neuroscience, where increasing evidence suggests that it coordinates neural dynamics across spatial and temporal scales and it is related to physiological and pathological states of the neural networks [6,8]. Besides, recent studies have highlighted the relevance of the CFC phenomenon associated to non-sinusoidal waveforms [9]. However, scarce studies have been devoted to analyze the CFC phenomenon emerging from non-sinusoidal dynamics characterized by a high content of harmonic spectral components. As a consequence, fundamental issues regarding the interpretations of the CFC patterns observed at the signal level remains open.

The basic mechanistic interpretation behind CFC is that independent oscillations interact hierarchically [10,11]. For instance, in bubble(s)-resonator systems, one oscillator constituted by a cavitation bubble, produces high-frequency acoustic waves with their phases modulated by the amplitude of low-frequency oscillations of a second oscillator, given by the standing sound wave developed within the acoustic chamber. It is worth noting that the cavitation bubbles are driven by the standing sound wave, however, they can be considered as independent oscillators taking into account the significantly different spatial and temporal scales involved in the dynamics of the acoustic chamber and the nonlinear oscillating bubble(s). The proper characterization and interpretation of the CFC patterns could pave the way to understand the dynamics and functions of the underlying mechanisms of the physical system under study. As a consequence, specialized signal processing techniques have been developed to detect and quantify the CFC phenomenon in noisy time series [12,14–16].

In spite of these advances, the standard CFC analysis from time series and its interpretation related to the underlaying physical mechanisms presents some fundamental issues [8,9,11]. The first concern has to do with whether the CFC patterns obtained from a given sensor are a true interaction reflecting a mechanistic process between two independent oscillators, or whether it might be a more trivial consequence of spectral correlations due to the non-sinusoidal waveform constituting the recorded time series [11]. In terms of telecoms engineering, the harmonic content constituting the spectrum of a quasi-periodic non-sinusoidal waveform with fundamental frequency f_0 can be though as a "carrier" given by the harmonic Nf_0, being N the harmonic number, and "sidebands" $(N-1)f_0$, $(N+1)f_0$. This spectral profile is known to produce a CFC pattern in the time domain (e.g, an amplitude-modulated signal) even when the underlying process generating the non-sinusoidal dynamics could be a single oscillator in a nonlinear regime, rather than a set of coupled oscillators [8,9,17]. Spurious CFC can be illustrated in considering different musical instruments playing the same note. Though the sound signals produced by each instrument share the same fundamental frequency, they have quite different harmonic and overtone content. These spectral components yield different CFC patterns in the time domain (e.g. different amplitude envelope of the sound signal). However, the spectral profile is a consequence of the individual oscillatory dynamics and does not necessarily imply the existence of interacting oscillators constituting each instrument. A second concern refers to whether the CFC pattern reflects a mechanistic causal coupling between the features involved (phase, amplitude, frequency) or just an indirect correlation (i.e. an epiphenomenon).

In this work we experimentally demonstrate that, as a consequence of the bubble(s)-resonator mechanistic interaction, "causal" CFC patterns are present in the bubble(s)-resonator dynamics in which the amplitude of the fundamental frequency component (f_0) effectively modulates the amplitude and relative phase of the harmonic components (Nf_0). Besides, we found the coexistence of "epiphenomenal" CFC patterns in which the link between modulating and modulated parameters represents a correlation rather than a causal connection. It is shown that these CFC patterns can be exploited to determine the presence, spatial stability and radial position of nonlinear oscillating bubble(s) trapped within the acoustic chamber. Potential applications of the proposed techniques are also discussed.

2. Apparatus and experimental method

The experiments were performed using a spherical acoustic chamber made of quartz (60 mm in outer diameter and 1 mm in thickness) described and characterized in Refs. [19–23,25]. The spherical flask was filled with a degassed sulfuric acid aqueous solution 85% *w/w* (SA85) with concentrations of dissolved gas (argon or xenon) in the range $0.001 \lesssim c_\infty/c_{sat} \lesssim 0.017$, where c_∞ and c_{sat} are the ambient and saturation gas concentrations, respectively. The resonance frequency of the acoustic chamber for the lowest order radially symmetric oscillation mode, with a pressure antinode near the geometrical center of the flask, was experimentally determined in $f_0 \approx$ 29.15 kHz.

The driving system was composed of four equal piezoceramics transducers made of PZT: lead zirconate titanate (20 mm in outer diameter, 5 mm of inner diameter and 4 mm in thickness). The four PZT drivers were glued to the outer wall of the resonator in diametrically opposed pairs as shown in Fig. 1. Two drivers (PZT_{LF}) were excited with the low-frequency electrical signal ($V_{LF} = V_0 \sin(2\pi f_{LF} t)$), while the remaining pair (PZT_{HF}) was used with the high-frequency driving signal ($V_{HF} = V_N \sin(2\pi (N f_{LF} + \delta f) t + \alpha)$ with $N \in \mathbb{N}$). Unless otherwise specified, in all the reported experiments the low-frequency driving V_{LF} was tuned to the resonance of the acoustic chamber first mode ($f_{LF} = f_0 \approx$ 29.15 kHz). A disc shaped piezoelectric ceramic microphone (MIC) was attached to the resonator wall in order to obtain a signal representative of the bubble(s)-resonator interaction in the oscillatory steady-state. The MIC provides an electrical signal proportional to the acceleration of the resonator wall. In particular, the amplitude of the fundamental frequency component (f_0) results proportional to the acoustic pressure applied at the center of the resonator ($P_{LF}(r = 0)$). In the experiments, the acoustic pressure field was set by controlling the frequencies (f_{LF}, Nf_{LF}, δf), relative phase (α) and amplitudes (V_0, V_N) of the electrical driving components, which keep a linear relation with those observed in the acoustic components provided by the MIC.

The bubbles were produced by acoustic cavitation near the center of the spherical resonator, were the main pressure antinode is located [25]. The radial position within the spherical chamber (r_b) and the spatial stability of the studied SL bubbles, were evaluated through photographs captured by the *Hitachi KP-F120* camera taking into account the curvature of the spherical resonator wall and the changes in the refractive index of the propagation media.

The collapse time of the bubbles (t_c), defined as the time interval between the zero crossing with negative slope of the acoustic pressure fundamental frequency component and the SL flash emission [18], was measured by a timer *Stanford Research Systems SR620*. The t_c value depends on the bubble ambient radius (R_0) and the acoustic pressure on the bubble ($P_{LF,b}$) [3], which are the coordinates of the bubble parameters space $P_{LF,b}$–R_0 [2]. A change in t_c value can be associated to modifications in the bubble radial dynamics $R(t)$ due to displacements of the bubble to regions of the acoustic field with different amplitudes ($P_{LF,b}$). As a consequence, assuming diffusive and shape stability of the bubble, monitoring the t_c is an alternative method to detect change in the bubble radial position (r_b) inside the spherical chamber.

The standard Mie scattering technique [28] was used to determine the temporal evolution of the bubble radius ($R(t)$). The scattered light was captured using an *Oriel 77340* phototube connected to a *Hewlett-Packard HP 54615B* oscilloscope. The experimental data traces were processed and fitted employing the numerical model of the bubble radial dynamics ($R(t)$) described in Ref. [2] which is based on the Rayleigh-Plesset-Keller equation (RPK). This model takes into account mass

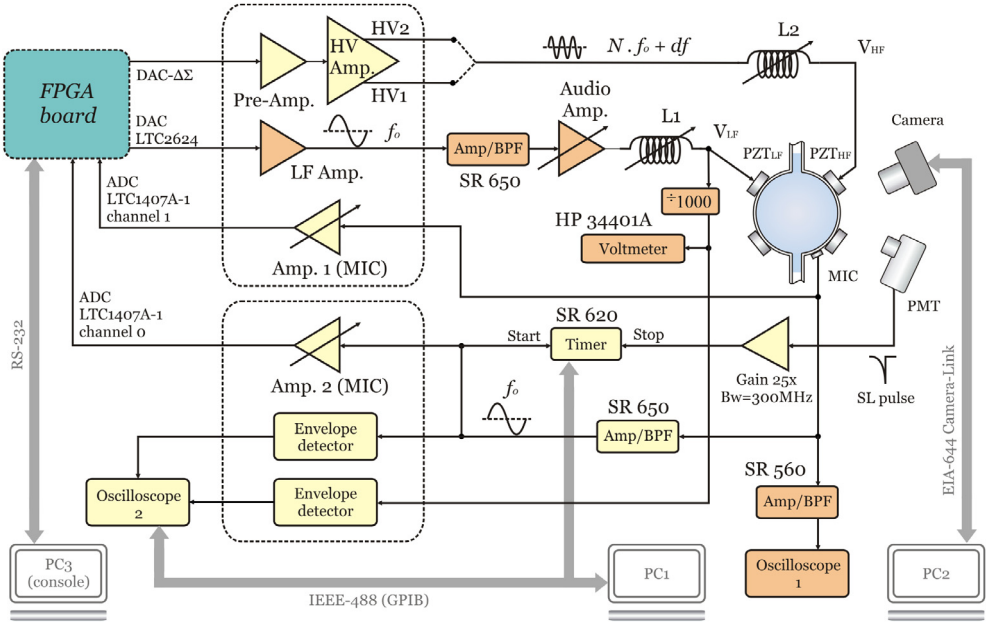

Fig. 1. Experimental setup used to characterize the resonator and bubble dynamics under single and bi-frequency drivings. Blocks in orange constitute the experimental arrangement used for the single-frequency driving experiments. For a detailed description of the instrumentation see A.

transfer effects at the bubble wall (e.g. evaporation and condensation). The physical properties of the liquid used in the simulations have been summarized in Table 1 of Ref. [26].

Further details about the instrumentation and electronics involved in the setup shown in Fig. 1, can be found in Appendix A.

2.1. Experiments

Three series of experiments were carried out using the setup shown in Fig. 1. In the first trial, single frequency driving (V_{LF}) was applied to PZT_{LF} transducers and the MIC signal was registered for several amplitudes of the electrical driving (V_0). For this, we used the instrumentation indicated by the orange colored blocks shown in Fig. 1. We first characterized the resonator in absence of bubbles to establish a reference case, and then we explored several SL scenarios in order to study the harmonic content in the bubble(s)-resonator dynamics. The obtained results are described in Section 4.1. In the second series of experiments, the amplitude of the single frequency driving (V_{LF}) was gradually increased to produce a radial displacement on the bubble position, induced by the primary Bjerknes force, starting from the center towards the wall of the acoustic chamber (i.e. positional instability) [18,23–26]. This allowed us to study the effect of the bubble radial position on the harmonics observed in the MIC signal. In a first approach, quasi-static ramps of V_0 were applied using the volume control knob of the audio amplifier (*Audio Amp.* in Fig. 1). Besides, the amplitude and relative phase of the harmonics present in the MIC signal were measured in real-time by means of the lock-in system described in Refs. Appendix A. The second approach was also performed using single frequency driving (V_{LF}) under several SL bubble scenarios, but in this case V_0 was increased in a sequence of discrete amplitude steps. In each step, the radial position of the SL bubble was also registered (see Fig. 7). The results of this experiment are described in Sections 4.2 and 4.3. For the third series of experiments, we used bi-frequency driving (V_{LF} + V_{HF}) to manipulate in real-time the harmonic content of the acoustic field and to analyze its influence on the bubble dynamics (radial, spatial and positional). In this case, the instrumentation indicated by the orange and yellow colored blocks shown in Fig. 1 was used. The results regarding the active manipulation of harmonics are described in Section 4.4.

3. Signal processing algorithms

In this Section we describe the algorithms implemented in hardware and software to analyze the harmonic content and CFC patterns associated to the bubble(s)-resonator dynamics.

3.1. Power spectral density

Power spectral density (PSD) estimates were computed using the modified periodogram method. Windowing in time domain was implemented using a Gaussian function in order to be able to compute the quadratic interpolation technique to obtain the spectral peaks coordinates (amplitude and frequency) [21]. Thresholding of the power spectrum at 3 times the median value of its amplitude was used for peaks detection.

3.2. Phase locking value

The quantification of CFC patterns was implemented using the phase locking value (PLV) algorithm described in [12–15]. Specifically, we computed the *PLV* as follows,

$$PLV = \frac{1}{N_s}\sum_{n=1}^{N_s} e^{j(N\phi_{LF}(n)-M\phi_{HF}(n))}, \tag{1}$$

where n is the discrete time index ($n \in \mathbb{Z}$), j is the imaginary unity, N_s is the number of samples of the time series, $\phi_{LF}(n)$ and $\phi_{HF}(n)$ are the phase time series computed from the band-pass filtered (BPF) version of the MIC signal ($x_{MIC}(n)$) by using the Hilbert transform, N and M are some integers. The *PLV* measure takes the value of 1 for perfect locking between the phase time series and 0 if they are completely desynchronized (for a sufficiently large number of samples N_s) [15]. The phase time series of Eq. 1 are obtained from the following procedure,

$$x_{LF}(n) = BPF_{LF}\{x_{MIC}(n)\} \tag{2}$$

$$x_{HF}(n) = BPF_{HF}\{x_{MIC}(n)\} \tag{3}$$

$$\phi_{LF}(n) = arg\,[x^{+}_{LF}(n)] \tag{4}$$

$$a_{HF}(n) = |x^{+}_{HF}(n)| \tag{5}$$

$$\phi_{HF}(n) = \begin{cases} arg\,[x^{+}_{HF}(n)], & \text{for PPC.} \\ arg\,[a^{+}_{HF}(n)], & \text{for PAC,} \end{cases} \quad (6)$$

where $BPF\{.\}$ denotes linear band-pass filtering around f^c with a bandwidth Bw. The BPFs were implemented in the frequency domain by multiplying the Fourier transform of the input signal by a Hann window and then, applying the inverse Fourier transform to get the band-pass filtered signal back in the time domain. It is worth noting that this particular filtering approach was used to effectively isolate the desired frequency components. In Eqs. (4)–(6), $x^{+}(n)$ denotes the analytic signal defined as $x^{+}(n) = x(n) + j\hat{x}(n)$ [29], where $\hat{x}(n)$ is the Hilbert transform of the original time series $x(n)$ (see Appendix B). For a band-limited signal $x(n)$, here guaranteed by the band-pass filtering in Eqs. 2 and 3, and if the BPFs satisfy $f^c \gg Bw$ results that the amplitude envelope $a(n)$ and phase time series $\phi(n)$ of the signal $x(n)$ are obtained by computing the module $|x^{+}(n)|$ and argument $arg\,[x^{+}(n)]$ of the analytic signal, respectively [29]. A graphical representation of the signals resulting from Eqs. (2)–(6) is given in Fig. 1 of Ref. [13].

In this work, the analysis was focused on the harmonic spectral components of the bubble(s)-resonator dynamics. Thus, in order to evaluate the phase-to-phase coupling (PPC), the band-pass filters $BPF_{LF}\{.\}$ and $BPF_{HF}\{.\}$ (Eqs. (2) and (3)) were configured with a null-to-null bandwidth of $Bw = f_0$ and centered at the fundamental frequency $f^c_{LF} = f_0$ $(M = 1)$ and its harmonics $f^c_{HF} = Nf_0$ $(1 \leqslant N \leqslant 42)$, respectively (see Fig. B.16 in Appendix B). The *PLV* quantity computed from Eq. 1, is the average of the complex vector of phase angle differences from which one can extract the magnitude and phase. Thus, in the case of PLV for PPC we introduce the notation,

$$PLV^{PPC}_N = I^{PPC}_N e^{j\Phi^{PPC}_N}, \quad (7)$$

where the module I^{PPC}_N reflects the intensity of the phase-phase coupling (i.e. the degree of phase synchronization) and Φ^{PPC}_N is the circular mean value of the relative phase between the signals $x_{LF}(n)$ and $x_{HF}(n)$ (see Eqs. (1)–(6)). On the other hand, to evaluate the phase-to-amplitude coupling (PAC) the BPF_{HF} filters were centered at $f^c_{HF} = (N + 0.5)f_0$ with $1 \leqslant N \leqslant 42$ and a null-to-null bandwidth of $Bw = 2f_0$ (see Fig. B.17 in Appendix B). In this case we have,

$$PLV^{PAC}_N = I^{PAC}_N e^{j\Phi^{PAC}_N}, \quad (8)$$

where Φ^{PAC}_N is the circular mean value of the relative phase between the signals $x_{LF}(n)$ and $a_{HF}(n)$ (see Eqs. (1)–(6)). The module I^{PAC}_N is the strength of the phase-amplitude coupling. Here, I^{PAC}_N is not a direct measure of the amplitude modulation depth, but rather, it reflects the degree of phase synchronization between the signals $x_{LF}(n)$ and $a_{HF}(n)$. It should be noted that the relative phase values Φ^{PPC}_N and Φ^{PAC}_N are insensitive to the phase transfer function associated to the electronics for MIC signal conditioning and acquisition, while the phase signals $\phi_{LF}(n)$ and $\phi_{LF}(n)$ do not (Eqs. 4 and 6).

The length of the MIC time-series collected in each measurement was ≈ 10 ms. Thus, Eqs. 1, 7 and 8 were computed over ≈ 300 cycles of the fundamental spectral component f_0. In all the cases, the MIC signal was z-scored to have the same zero mean and unit variance before processing it through Eqs. (2)–(6). In order to mitigate edge artifacts due to the transient response of the BPFs and the computation of the analytic signals, we implemented the time series reflection procedure described in Ref. [16]. Briefly, time series are reversed in time, concatenated to both ends of the real-data time series, analyses are performed (Eqs. 2, 3 or B.1), and then the reflected data are trimmed. Additionally, a surrogate control analysis was implemented to obtain a statistical significance threshold ($p < 0.05$) for the I^{PPC}_N and I^{PAC}_N values [16].

3.3. FPGA-based lock-in system

The PLV algorithm described above was used to quantify the PPC and PAC patterns from the registered MIC signal in a subsequent processing of the experimental data. On the other hand, the FPGA-based lock-in system (*FPGA board* in Fig. 1) allowed us to obtain, in real-time, the amplitude and phase relative to the fundamental frequency component of up to 5 frequencies at ≈4 sps. The digital processing algorithms involved in the FPGA-based system have been previously described in Refs. [21,27]. The lock-in system provided amplitude A^{LI}_N and phase Φ^{LI}_N values for the harmonics Nf_0, averaged over a time interval of $5\tau \approx$ 250 ms (≈ 730 cycles of f_0) with an equivalent noise bandwidth $ENBW = 2f_{-3dB} \approx$ 40 Hz, both determined by the low-pass filter of the system ($\tau \approx$ 50 ms, $f_{-3dB} \approx$ 20 Hz). The Φ^{LI}_N values were normalized with respect to the fundamental frequency component f_0 $(M = 1)$. As a consequence, Φ^{LI}_N and Φ^{PPC}_N have opposite signs (see Eq. (1)).

4. Results and discussion

The discussion of the results and the reasoning behind the conclusions are outlined as follows. In Section 4.1 we discuss the nature of harmonics observed in the nonlinear dynamics of the acoustic resonator. Sections 4.2 and 4.3 are devoted to analyze the CFC patterns observed in the system response produced by the bubble(s)-resonator interaction. In Section 4.4, bi-frequency driving is used to study the effect of high-frequency harmonics, produced intrinsically by the bubble(s)-resonator system, on the bubble dynamics (radial, spatial and positional).

4.1. Harmonics in the system dynamics

The first series of experiments were aimed to analyze the harmonics present in the acoustic field developed within the spherical resonator under single frequency driving (orange colored blocks in Fig. 1). For these experiments we verified that the PSD of the electrical signal applied to the PZT_{LF} transducers, do no show harmonic frequencies peaks detectable above the threshold at 3 times the median value of PSD amplitude (see Section 3.1). This remains valid for V_0 values well above the maximum driving amplitude used in the experiments reported here ($V_0 \approx$ 400 Vrms). Fig. 2 shows the PSDs of the MIC signals corresponding to four scenarios [1]: (*I.- No-bubble*) Absence of bubbles within the liquid-filled spherical shell, (*II.- Non-moving SBSL*) Spatially stable (without pseudo-orbits) single sonoluminescent bubble, (*III.- Moving SBSL*) Single sonoluminescent bubble describing pseudo-orbits, and (*IV.- Moving MBSL*) Multiple spatially unstable sonoluminescent bubbles.

In these acoustic scenarios, we observed non-sinusoidal shape of oscillatory waveforms constituting the MIC signal, which was characterized by a high content of harmonic spectral components. Besides, the periodicity of these oscillations was altered by the presence of noise and jitter produced by the bubble(s) movement in pseudo-orbits. The latter was traduced in a widening of the harmonic spectral peaks (see Fig. 2). Thus, the acoustic scenarios analyzed in this work were characterized by a quasi-periodic non-sinusoidal dynamics.

Spatially stable SL bubbles were produced by using a liquid with low dissolved noncondensible gas concentrations (i.e. $c_\infty/c_{sat} < 0.01$ of argon or xenon in SA85). For higher concentrations of dissolved gas ($c_\infty/c_{sat} \geqslant 0.01$) spatially unstable SL bubbles moving in pseudo-orbits were obtained due to the action of the history force [21,23,24]. Insets (A) and (B) of Fig. 3 illustrate the typical behavior of spatially stable and unstable SL bubbles respectively, for an increasing ramp of the driving amplitude V_0. By applying the peak detection method described in Section 3.1 on the power spectra shown in Fig. 2, it was obtained that frequencies of the detected spectral peaks match those of the harmonics Nf_0 of the fundamental component f_0 with a difference less than 0.1% [1,21]. In the *No-bubble* scenario of Fig. 2, spectral harmonic peaks with amplitudes greater than $\approx -40dB$ relative to the fundamental component (f_0) are observed for $N \lesssim 12$. These nonlinear harmonics Nf_0 for $N < 15$ in absence of bubbles, are produced by the excitation of acoustic

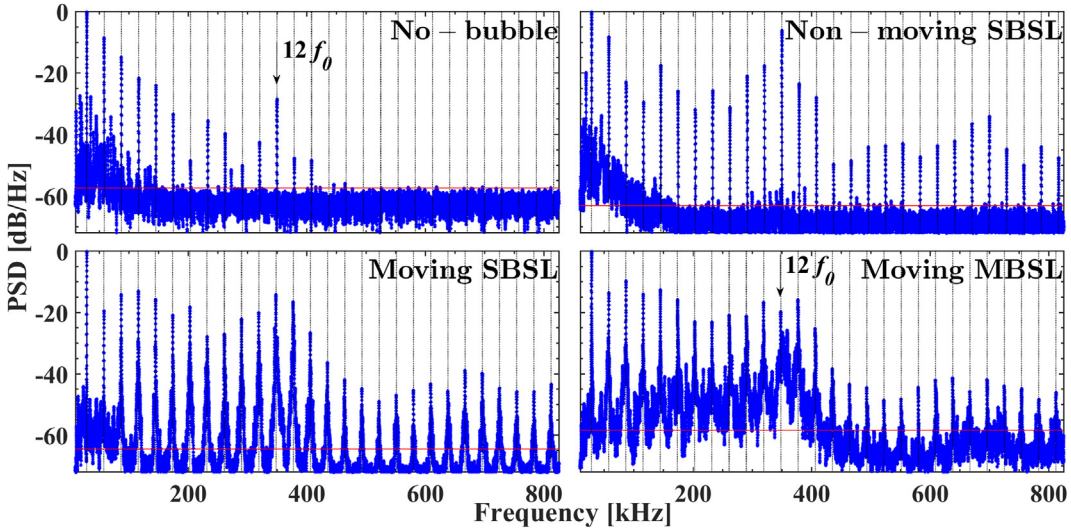

Fig. 2. Power spectra (PSD) computed from MIC signals corresponding to the four nonlinear acoustic scenarios: *No-bubble* ($V_0 \approx$ 200 Vrms), *Non-moving SBSL* ($V_0 \approx$ 196 Vrms), *Moving SBSL* ($V_0 \approx$ 204 Vrms) and *Moving MBSL* ($V_0 \approx$ 260 Vrms). Each graph shows the average between 4 and 10 PSD estimates computed using the modified periodogram method with a Gaussian window in time domain. The horizontal solid lines (red) are the thresholds at 3 times the median value of the PSD amplitude, which were used for the peaks detection. The vertical dashed lines indicates the exact position of the harmonic frequencies (Nf_0). (For interpretation of the references to colour in this figure legend, the reader is referred to the web version of this article.)

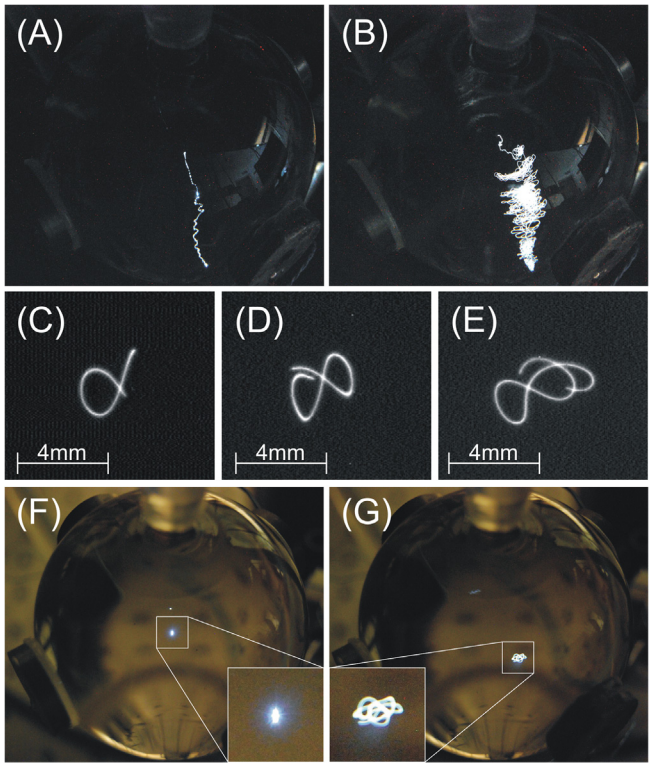

Fig. 3. Photographs of argon and xenon SL bubbles in SA85. Insets (A) and (B) correspond to spatially stable ($c_\infty/c_{sat} < 0.01$) and unstable ($c_\infty/c_{sat} \geqslant 0.01$) xenon SL bubbles respectively, in the case of single-frequency driving ($f_0 \approx$ 29.15 kHz). The photographs were taken with an exposure time of 30 s. during a ramp of the driving amplitude V_0. Photographs (C), (D) and (E) show typical pseudo-orbits of size ≈ 4 mm, described by an argon SL bubble in SA85 (single frequency driving and $c_\infty/c_{sat} \approx 0.016$) taken with exposure times of 150 ms, 250 ms and 350 ms respectively. Photographic montages (F) and (G) show xenon SL bubbles in SA85 with $c_\infty/c_{sat} \approx 0.03$. The exposure time of both photographs was 1 s. Photograph (G) corresponds to a spatially unstable SL bubble under single-frequency driving (f_0). Photograph (F) shows the same SL bubble spatially stabilized using bi-frequency driving (f_0 and $7f_0$). The bright objects outside the framed area are produced by the reflection of the actual SL bubble in the inner wall of the spherical flask.

modes associated to the liquid-filled resonator, and are not related to the elastic modes of the spherical shell, i.e. air-filled resonator (see Fig. 4 in Ref. [1]). The measured quality factor (Q) of the first radially-symmetric acoustic mode of the liquid-filled shell is $Q \approx$ 250 [21], resulting in a full-width half-power (-3 dB) bandwidth of $Bw_0 = f_0/Q \approx$ 117 Hz. It was found that by detuning the driving signal well above or below the Bw_0 of the resonator ($f_{LF} \approx f_0 \pm 10Bw_0$) and keeping the driving amplitude V_0 unchanged, those harmonic peaks present in the *No-bubble* scenario were attenuated in more than 2 orders of magnitude for $N = 2$ and attenuations greater than 4 orders of magnitude were observed for $N \geqslant 3$ [22]. These results are shown in Fig. 4. This evidence suggest that the amplitudes of harmonic peaks obtained in the *No-bubble* scenario, are not completely explained by only considering a nonlinear behavior of the acoustic resonator. Instead, it appears that to account for the presence of the harmonic peaks, acoustic energy coupling from the first mode to others high-frequency modes (not necessarily radially symmetric), has to be considered besides the nonlinear behavior of the resonator. This hypothesis is consistent with the observed amplitude of the harmonic peaks in both resonance ($f_{LF} = f_0$) and off-resonance ($f_{LF} \approx f_0 \pm 10Bw_0$) driving conditions discussed above. It is important to note that the boundary condition imposed by the elastic properties of a solid shell of finite thickness, produces a set of non-harmonic eigenfrequencies for the radially symmetric modes [19]. However, the coupling between the first mode with other acoustic modes around harmonic frequencies is favored by the quadratic growth of the number of spherical normal modes with the frequency [21] and by the degeneracy of the non-radially symmetric modes [4]. In absence of bubbles, acoustic energy is transferred from the fundamental spectral component (f_0) to its harmonics (Nf_0) as the driving amplitude is increased ($V_{LF} \gtrsim$ 100 Vrms). Specifically, the decrease in the fundamental component amplitude matches the observed increase of the summed amplitudes of harmonics in the range $2 \leqslant N \leqslant 5$ (see Fig. 3 of Ref. [1]). This observation support the hypothesis of inter-mode coupling in which high-frequency modes drain acoustic energy from the resonator first mode, reducing the oscillatory amplitude of the latter.

The results discussed above provide quite strong experimental evidence indicating that in absence of bubbles, the interaction among acoustic modes of the spherical resonator, coupled via 1: N internal resonances, plays a relevant role in producing the nonlinear spectral harmonics (Nf_0) present in the resonator dynamics. On the other hand,

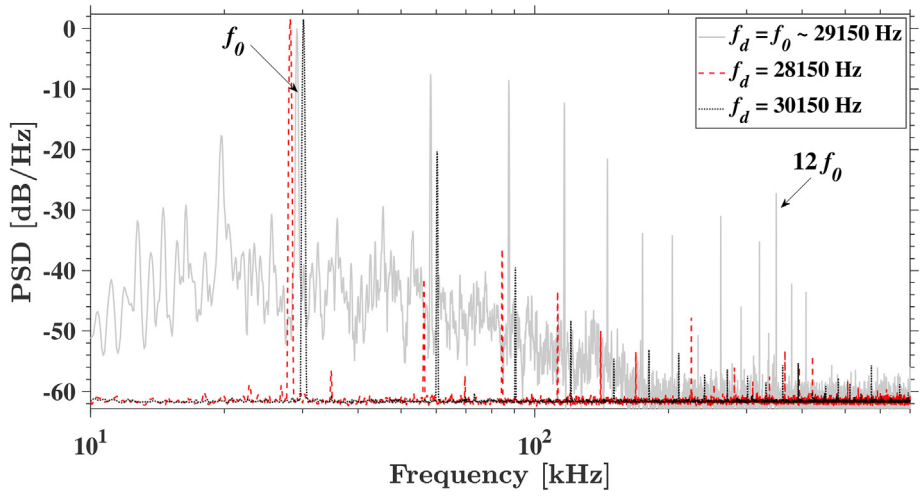

Fig. 4. Power spectra (PSD) computed from MIC signals corresponding to the response of the acoustic resonator in absence of bubbles. The amplitude of the single-frequency driving $V_0 \approx 300$ Vrms was kept unchanged for the three spectra. The frequency of the driving was set at $f_{LF} = f_0 \approx 29.15$ kHz (gray solid line), $f_{LF} \approx 28.15$ kHz (red dashed line) and $f_{LF} \approx 30.15$ kHz (black doted line). Detuning the driving signal well above or below the bandwidth of the first radially-symmetric acoustic mode ($Bw_0 = f_0/Q \approx 117$ Hz), produce the attenuation of harmonic peaks in more than 2 orders of magnitude for $2f_0$ and attenuations greater than 4 orders of magnitude occurs for harmonics above $3f_0$. (For interpretation of the references to colour in this figure legend, the reader is referred to the web version of this article.)

the SBSL and MBSL scenarios displayed in Fig. 2 (also in Fig. 4 of Ref. [1]) show that, the periodic shock-wave emission from the sonoluminescent bubble(s) acoustically trapped within the resonator produces high-frequency harmonics well above $15f_0$, which were not observed in absence of bubbles [4,19,21,22].

4.2. Phase-to-phase cross-frequency coupling analysis

In this Section we discuss the experiments designed to explore the CFC patterns and the mechanistic relation between the bubble(s) radial position and the intrinsic harmonics of the bubble(s)-resonator dynamics discussed in Section 4.1. The experiments were carried out using single frequency driving (V_{LF}) under several SL bubble scenarios. Quasi-static ramps of V_0 were applied to induce the bubble(s) displacement from the center towards the wall of the acoustic chamber, as shown in Fig. 3(A) and (B). During these ramps, the amplitude A_N^{LI} and phase Φ_N^{LI} of the harmonics Nf_0 present in the MIC signal were measured in real-time by the lock-in system described in Section 3.3 and Appendix A (FPGA board in Fig. 1). As an example, Fig. 5 shows the bubble radial position r_b together with A_{12}^{LI} and Φ_{12}^{LI} for the harmonic $12f_0$, as a function of the acoustic pressure at the resonator center $P_{LF}(r = 0)$ produced by a quasi-static ramp of V_0. In the *Non-moving SBSL* scenario (i.e. Fig. 3(A)) shown in Fig. 5, it is possible to distinguish a regular structure in the time evolution of A_{12}^{LI}. Besides, jumps in Φ_{12}^{LI} occurring around the local minima of A_{12}^{LI}, indicate that the behavior shown in Fig. 5 is likely produced by the excitation of an acoustic mode of the resonator, as the bubble pass through the pressure nodes and antinodes associated to that normal mode. Taking into account the reciprocity principle [31], the amplitude profile shown in Fig. 5 would also have been observed from a hydrophone located at the bubble position while

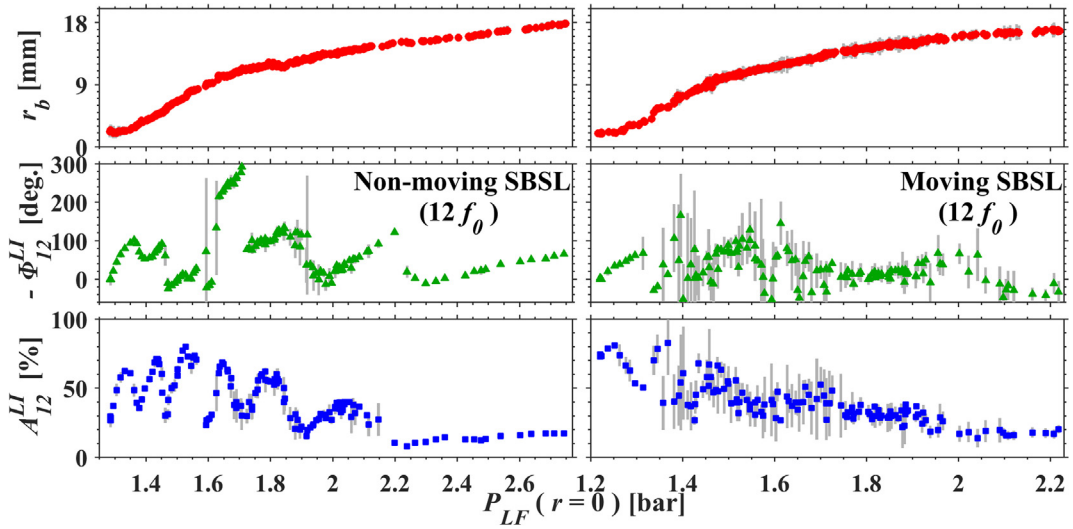

Fig. 5. Bubble radial position (r_b) together with the amplitude (A_{12}^{LI}) and phase (Φ_{12}^{LI}) of the harmonic $12f_0$ present in the MIC signal, as a function of the acoustic pressure at the resonator center $P_{LF}(r = 0)$ produced by a quasi-static ramp of V_0. The values A_{12}^{LI} and Φ_{12}^{LI} were measured in real-time by the lock-in system described in A, and normalized with respect to those of the fundamental frequency component. (Upper graphs) Bubble radial displacement induced by the primary Bjerknes force. The error bars are the standard deviation of 3 measurements at each point. (Middle graphs) Amplitude-to-phase coupling (APC) in which the amplitude of the fundamental frequency component (P_{LF}) modulates the phase of the harmonic $12f_0$. (Bottom graphs) Amplitude-to-amplitude coupling (AAC) in which the amplitude of the fundamental frequency component (P_{LF}) modulates the amplitude of the harmonic $12f_0$.

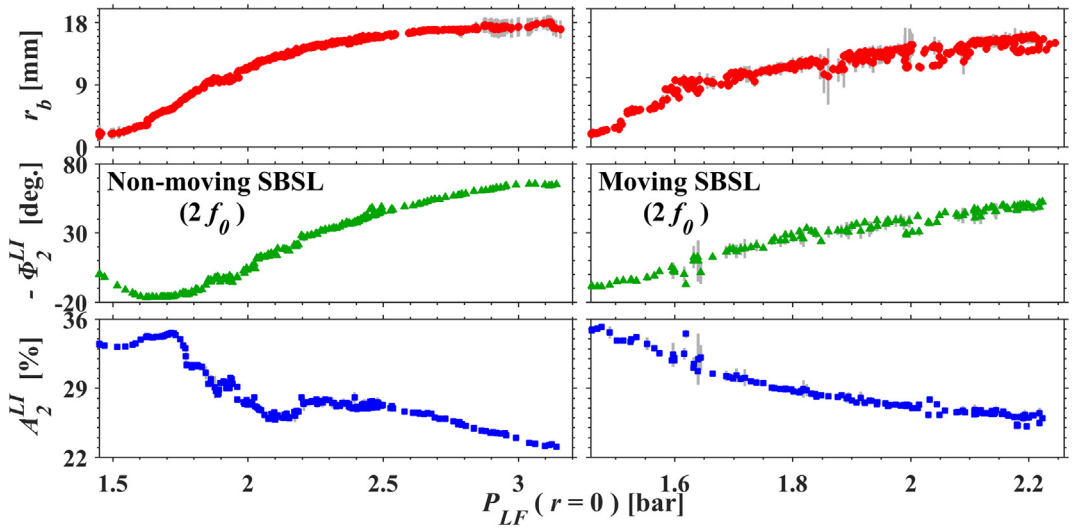

Fig. 6. Bubble radial position (r_b) together with the amplitude (A_2^{LI}) and phase (Φ_2^{LI}) of the harmonic $2f_0$ present in the MIC signal, as a function of the acoustic pressure at the resonator center $P_{LF}(r = 0)$ produced by a quasi-static ramp of V_0. Same experimental conditions as described in the caption of Fig. 5.

externally driving the same normal mode associated to the harmonic $12f_0$ using the PZT transducers. Fig. 5 shows that in both, A_{12}^{LI} and Φ_{12}^{LI}, the regular structure is significantly distorted by the bubble movement in pseudo-orbits (*Moving SBSL* scenario, i.e. Fig. 3 (B)). Similar results have been obtained for other harmonic components like $3f_0$ and $7f_0$ (not shown). In the case of the harmonic $2f_0$ shown in Fig. 6, the displacement of the bubble is accompanied by a monotonic increase of $-\Phi_2^{LI}$ in both, *Non-moving SBSL* and *Moving SBSL* scenarios.

Figs. 5 and 6 show that the amplitude of the fundamental frequency component ($P_{LF}(r = 0)$), modulates the amplitude and phase of other spectral components (Nf_0), which correspond to amplitude-to-amplitude (AAC) and amplitude-to-phase (APC) cross-frequency couplings, respectively. The APC and AAC patterns shown in Figs. 5 and 6 admit the following mechanistic causal explanation: The ramp of P_{LF} induces the observed displacement of the bubble(s) (i.e. positional instability) [18,23–26]. This change in r_b modifies the interaction between bubble acoustic emission and the normal modes of the resonator, which in turn yields a change in the amplitude and phase of the intrinsic harmonics observed in the MIC signal. Further experimental evidence supporting this hypothesis is discussed in Section 4.4.

Remarkably, Fig. 5 shows that for the *Non-moving SBSL* scenario, small changes in the bubble radial position around the pressure nodes associated to the excited high-frequency acoustic mode ($12f_0$), produced large changes in the relative phase of the corresponding harmonic. These "jumps" in the harmonic phase were better resolved in the case of low-frequency harmonics like $3f_0$ and $7f_0$, which present smoother amplitude and phase profiles during the V_0 ramps (not shown). This behavior can be exploited to monitor the position of an spatially stable bubble relative to the location of pressure nodes corresponding to different acoustic modes. It should be noted that the specific way in which the amplitude and phase of the harmonics change as functions of the bubble displacement, depends on the particular characteristics of the bubble(s)-resonator system, such as the shape and the physical properties of the solid shell, the fluids and the emitting source (i.e. bubble radial dynamics). In our spherical resonator, the harmonic $2f_0$ results of particular interest since a rather linear dependence of Φ_2^{LI} with r_b is maintained from the center to near the spherical wall of the resonator. Besides, Fig. 6 shows that the dependence of Φ_2^{LI} with r_b is not significantly affected by the movement of the SL bubble in pseudo-orbits. As a consequence, Φ_2^{LI} can be used to estimate r_b in the case of spatially stable as well as unstable bubbles.

The results based on the measurements obtained in real-time using the lock-in system (Figs. 5 and 6) were complemented by an alternative approach. Namely, V_0 was increased in a sequence of discrete amplitude steps while registering the MIC signal and the bubble radial position for a *Non-moving SBSL* scenario. Fig. 7 shows the registered positions of the SL bubble corresponding to each step of V_0. The length of the MIC time-series collected in each measurement was $\approx$ 10 ms corresponding to $\approx$300 cycles of the fundamental spectral component f_0. The MIC signal was subsequently processed using the PLV algorithm (Eqs. (1)–(8), (B.1)). In order to evaluate the degree of phase synchronization between the harmonics Nf_0 and the fundamental frequency component f_0, Eqs. (2) and (3) of the PLV algorithm were implemented using the filters configuration depicted in Fig. B.16 of Appendix B (i.e. PLV for PPC). Fig. 8 shows Φ_2^{PPC} as a function of r_b. The results shown in Fig. 8 are consistent with those shown in Fig. 6, confirming the dependence of the relative phase of the harmonic $2f_0$ with the bubble radial position r_b. For each measurement shown in Fig. 8, a high degree of phase

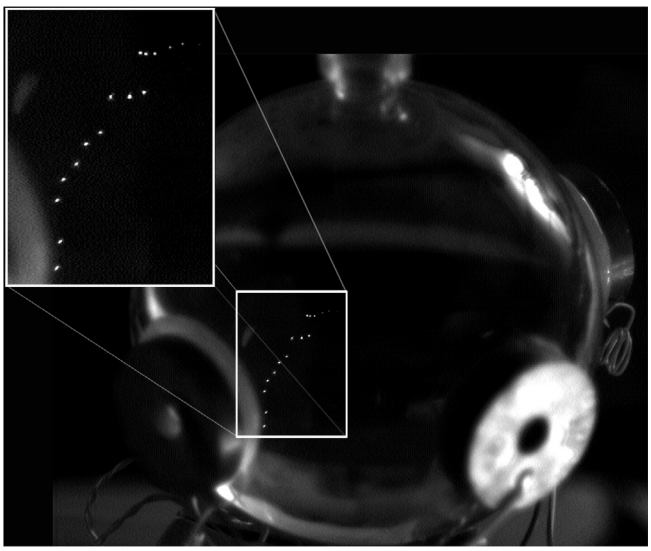

Fig. 7. Photographic montage of a spatially stable argon SL bubble under single-frequency driving in SA85. The image is a combination of 16 photographs taken with an increasing driving amplitude (V_0) under identical experimental conditions, being the bubbles positioned closer to the center of the resonator the ones with lower driving voltages. The driving frequency was fixed in f_0 = 29.16 kHz and the dissolved argon concentration in the liquid was $c_\infty/c_{sat} \lesssim 0.01$.

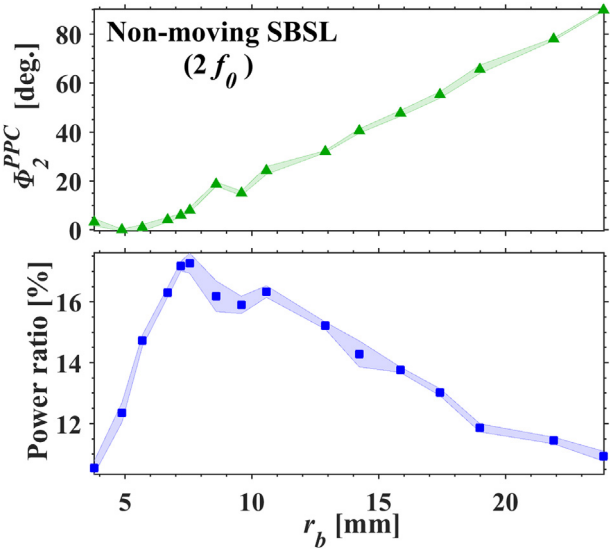

Fig. 8. Phase of the PLV_2^{PPC} (Φ_2^{PPC}), together with the relative power of the harmonic $2f_0$ as functions of the bubble radial position (r_b). In all the measurement shown, a high degree of phase synchronization was obtained ($I_2^{PPC} \approx 1$). The markers correspond to the mean value of ≈ 5 measurements at each point and the shaded error bars represents the absolute difference between the extreme values (max and min). The measurements were obtained by processing the MIC signals corresponding to the bubble positions shown in Fig. 7. The bottom graph shows the power of the band-pass filtered MIC signal around $2f_0$ relative to the power of the fundamental frequency component. The power ratio was computed using the BPFs configuration depicted in Fig. B.16 of Appendix B.

synchronization ($I_2^{PPC} \approx 1$) was obtained. Additionally, the statistical significance ($p \ll 0.05$) of this I_2^{PPC} values was verified by implementing a surrogate control analysis [16].

Fig. 9 shows the I_N^{PPC} values computed for the *No-bubble* case and different SL bubble scenarios. Tacking into account that the harmonics are perfectly phase locked with the fundamental frequency component, one would expect a phase-phase coupling strength of $I_N^{PPC} = 1$ in absence of noise. On the contrary, the background noise distort the phase time series $\phi_{LF}(n)$ and $\phi_{HF}(n)$ (Eqs. 4 and 6) from the ideal sawtooth waveform producing $I_N^{PPC} < 1$. As a consequence, the resulting I_N^{PPC} value depends on the relative amplitude of the harmonic spectral component with respect to the background noise level [15]. In particular, the harmonic spectral components $N = 7;10$ and $N \geq 15$ for the *No-bubble* case shown in Fig. 9 produce $I_N^{PPC} < 0.5$ due to the fact that their amplitudes are comparable to the noise floor level (see Fig. 2). The same behavior ($I_N^{PPC} < 0.5$) is obtained for the harmonics $N > 35$ corresponding to the *Non-moving SBSL* case shown in Fig. 9. Besides, in this scenario the presence of the spatially stable bubble increase the harmonics amplitude producing high phase-phase synchronization ($I_N^{PPC} > 0.5$) for harmonic numbers $2 \leqslant N \leqslant 35$.

In the *Moving SBSL* and *Moving MBSL* scenarios, the MIC signal used to compute the PLV_N^{PPC} (≈ 10 ms in length), includes the system response for slightly different positions of the oscillating bubbles due to their movement in pseudo-orbits (size ≈ 4 mm and period ≈ 200 ms, see insets (C), (D) and (E) in Fig. 3). Thus, the spatial instability of the oscillating bubbles increase the probability of excite several non-radially symmetric modes in the time window of the MIC signal. The latter produce a widening of the harmonic spectral peaks (see Fig. 2), since the degeneracy of the non-radially symmetric modes is lifted by shape perturbations of the shell, increasing the number of non-harmonic eigenfrequencies [19]. This situation is aggravated in considering several MIC time series since the bubble(s) position variability across trials is determined by the size of the pseudo-orbits (≈ 3 mm). As a result, Fig. 9 shows that the I_N^{PPC} values present a higher dispersion and decay more abruptly for $N > 2$ in the *Moving SBSL* and *Moving MBSL* scenarios, when compared to the *Non-moving SBSL* case. This is consistent with the results shown in Figs. 6 and 5 for the *Moving SBSL* case. The results shown in Figs. 5, 6 and 9 suggest that the bubble(s) spatial stability can be inferred by monitoring the CFC patterns present in the MIC signal (e.g. dispersion of the PLV_N^{PPC} values). It is important to note that in the *No-bubble* and *Non-moving SBSL* scenarios, a value of $I_2^{PPC} \approx 1$ was obtained for the harmonic $2f_0$ (see Fig. 9). However, Φ_2^{PPC} in the *No-bubble* case presents a much weaker dependence with V_0 than that observed in presence of SL bubble(s) (see below the discussion in connection with Figs. 10–12).

When a large number of SL bubbles are trapped within the acoustic chamber, they form an ellipsoidally-shaped tridimensional array [25], independently of their spatial stability. Besides, Rosselló et al. [25] have experimentally shown that the dimensions of these hollow clusters of bubbles are mainly determined by the primary Bjerknes force

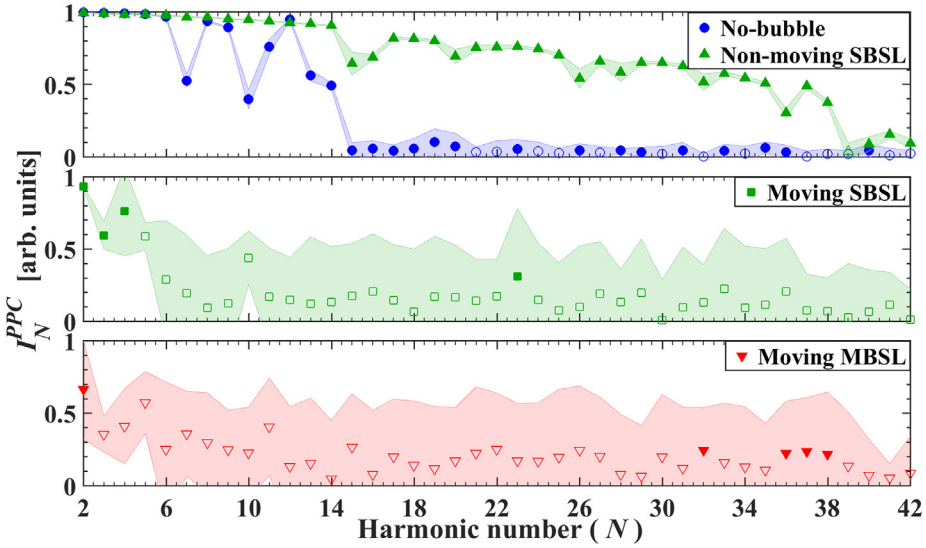

Fig. 9. Module of the phase locking values for PPC as a function of the harmonic number for several acoustic scenarios: *No-bubble* ($V_0 \approx$ 200 Vrms), *Non-moving SBSL* ($V_0 \approx$ 196 Vrms), *Moving SBSL* ($V_0 \approx$ 204 Vrms) and *Moving MBSL* ($V_0 \approx$ 260 Vrms). The markers result from the average between 4 to 10 measurements at each point and the shaded error bars represent the absolute difference between the extreme values (max and min). Filled and empty markers represent values of I_N^{PPC} above and below the statistical significance threshold ($p < 0.05$), respectively.

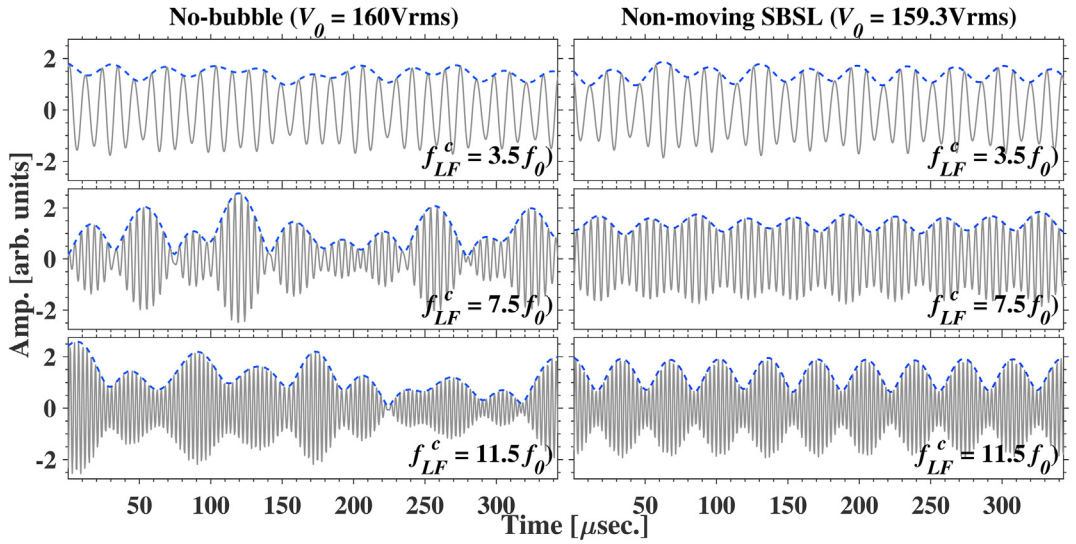

Fig. 10. Band-pass filtered MIC signals around $f_{HF}^c = (N + 0.5)f_0$ with a bandwidth of $Bw = 2f_0$. (Right graph) The amplitude envelope $a_{HF}(n)$ (dashed line) corresponding to the *Non-moving SBSL* case presents a regular, quasi-periodic time evolution mainly determined by f_0, i.e. the frequency difference between the harmonic components within the pass-band of the filters (see Fig. B.17 in Appendix B). (Left graph) The amplitude envelope for the *No-bubble* case undergo irregular fluctuations, that is, the amplitude modulation depth changes over time.

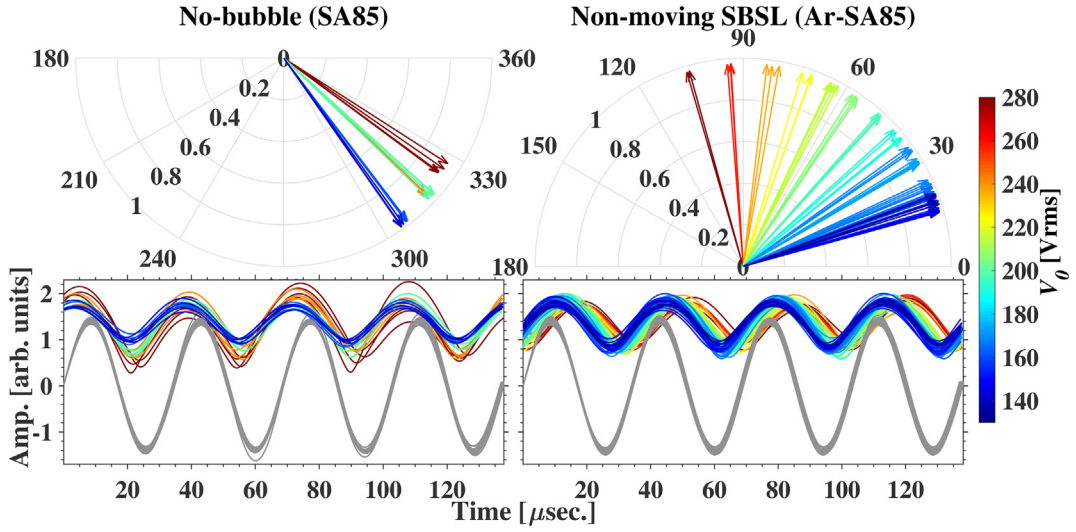

Fig. 11. Phase locking values for PAC parametrized with the driving amplitude V_0. Pseudocolor scale represents driving amplitude V_0 values shown at right. (Upper graphs) Polar plots of PLV_1^{PAC} phasors computed from the amplitude envelopes shown in lower graphs. The phasors length indicate the strength of the coupling ($I_1^{PAC} \approx 1$). (Lower graphs) Fundamental frequency components (solid gray lines) and amplitude envelopes $a_{HF}(n)$ (color-coded lines) computed from the band-pass filtered MIC signals around $f_{HF}^c = 1.5f_0$ with a bandwidth of $Bw = 2f_0$. The measurements for the *Non-moving SBSL* case were obtained by processing the MIC signals corresponding to the bubble positions shown in Fig. 7. (For interpretation of the references to colour in this figure legend, the reader is referred to the web version of this article.)

(positional instability). The technique proposed in this work, based on monitoring the phase of a low-frequency harmonic (e.g. $2f_0$) could be also applicable to estimate the mean radial bubble position even in the case of multi-bubble systems. However, it should be taken into account that I_N^{PPC} decays more abruptly for $N > 2$ in the *Moving SBSL* and *Moving MBSL* scenarios, and that the PLV^{PPC} values (module and phase) present a higher dispersion when compared to the *Non-moving SBSL* case (see Figs. 5, 6 and 9).

4.3. Phase-to-amplitude cross-frequency coupling analysis

In the following, the analysis is focused on the phase-to-amplitude coupling to study in more detail the nature of the CFC patterns, in presence and absence of bubbles within the acoustic chamber. The MIC signals corresponding to the SL bubble positions shown in Fig. 7 were processed using the PLV algorithm with the filter configuration depicted in Fig. B.17 of Appendix B (i.e. PLV for PAC). Fig. 10 shows the resulting band-pass filtered MIC signals for BPFs centered at $3.5f_0$, $7.5f_0$ and $11.5f_0$. The amplitude envelopes $a_{HF}(n)$ corresponding to the *Non-moving SBSL* case present a constant amplitude modulation depth with quasi-periodic time evolution mainly determined by f_0. The latter, is in turn given by the frequency difference between the harmonic components within the pass-band of the filters (see Fig. B.17 in Appendix B). On the other hand, the amplitude envelopes for the *No-bubble* scenario undergo irregular fluctuations, that is, the amplitude modulation depth changes over time.

It should be noted that, in presence of bubbles, the low-frequency harmonics ($N \lesssim 15$) observed in the MIC signal are the result of an interplay between the nonlinear behavior of the resonator and the

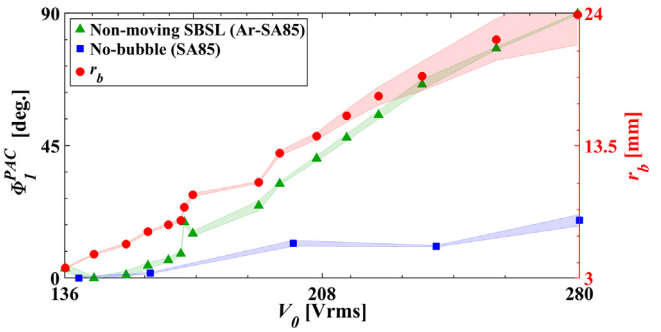

Fig. 12. Phase locking values for PAC as a function of the driving amplitude V_0. The Φ_1^{PAC} values, corresponding to the same PLV_1^{PAC} phasors presented in Fig. 11, are shown superimposed to the bubble radial position r_b. The markers correspond to the mean value of ≈ 5 measurements at each point and the shaded error bars represent the absolute difference between the extreme values (max and min).

acoustic emission of the bubbles. In line with this, the results shown in Fig. 10 suggest that the SL bubble acts as a pacemaker stabilizing the phase and amplitude of these harmonic components. This behavior can be exploited as a technique to determine the presence of nonlinear oscillating bubbles within acoustic chambers. Specifically, by monitoring the MIC signal band-pass filtered around low-frequency harmonics (e.g, BPFs centered at $3.5f_0$ with $Bw = 2f_0$), the presence of the bubble can be inferred from a constant amplitude modulation depth over time. Similar results to those shown in Fig. 10 were obtained for single and multiple bubbles with pseudo-orbital movement, and even for moving bubbles in a non-SL regime (not shown). The latter indicates that the proposed method is robust enough to be used in a variety of acoustic scenarios.

If the harmonic components f_0 and $2f_0$ are assumed to have similar constant amplitudes, their relative phase can be estimated from the amplitude envelope $a_{HF}(n)$ corresponding to the BPF centered at $1.5f_0$, that is, $\Phi_1^{PAC} \approx \Phi_2^{PPC}$ (see Eqs. (B.2)–(B.5) and Fig. B.17 in Appendix B). Fig. 11 shows the amplitude envelopes $a_{HF}(n)$, obtained from the BPF centered at $1.5f_0$ ($Bw = 2f_0$), as a function of the driving amplitude V_0. The PLV_1^{PAC} phasors computed from those amplitudes envelopes are depicted in the polar diagrams of Fig. 11. The phase Φ_1^{PAC} of these PLV_1^{PAC} phasors reflect the phase precession of $a_{HF}(n)$ shown in the lower graph of Fig. 11. The *Non-moving SBSL* case presented in Fig. 11 correspond to the SL bubble positions displayed in Fig. 7. Fig. 11 shows that, for the same excursion range of the driving amplitude (V_0), the angular range covered by Φ_1^{PAC} associated to the *Non-moving SBSL* case is four times larger than that corresponding to the *No-bubble* case. Fig. 12 shows Φ_1^{PAC} corresponding to the same cases presented in Fig. 11 together with the bubble radial position r_b. The results displayed in Fig. 12 associated to PLV_1^{PAC} are consistent with those presented in Fig. 8 obtained with PLV_2^{PPC}. These results reveal that the bubble radial position r_b can be estimated by processing low-frequency harmonics ($\approx 2f_0$) with the PLV algorithm configured for PPC or PAC (Figs. B.16 and B.17 in Appendix B).

In Sections 4.2 and 4.3, evidence has been presented showing the coexistence of "spurious" (*No-bubble* case in Figs. 9 and 10), "causal" (Figs. 5 and 6) and "epiphenomenal" (Figs. 8, 11 and 12) CFC patterns in the bubble(s)-resonator dynamics. In particular, the CFC patterns (PPC and PAC) observed in the *No-bubble* case are "spurious" in the sense that they emerge from the nonlinear dynamics of the acoustic chamber, and are not related to the interaction between individual oscillators. On the other hand, the characteristics of the "non-spurious" CFC patterns ("causal" and "epiphenomenal") associated to the bubble (s)-resonator interaction are summarized in Table 1. The amplitude of the acoustic pressure field (P_{LF}) imposed by the external driving (V_{LF}), constitutes the modulating parameter for the AAC and APC couplings. The balance of added mass and Bjerknes hydrodynamic forces

Table 1
Summary of the cross-frequency patterns observed in the bubble(s)-resonator dynamics.

Coupling name	Modulating parameter	Link	Modulated parameter	Link type
APC	Amp. (f_0)	$\longrightarrow r_b \overrightarrow{\not\leftarrow}$	Phase (Nf_0)	Causal connection
AAC	Amp. (f_0)	$\longrightarrow r_b \overrightarrow{\not\leftarrow}$	Amp. (Nf_0)	Causal connection
PPC	Phase (f_0)	$\leftrightarrow$	Phase (Nf_0)	Correlation
PAC	Phase (f_0)	$\leftrightarrow$	Amp. (Nf_0)	Correlation

determine the bubble(s) radial position in all the cases studied: single or multiple bubbles spatially stable or unstable, where in the latter case (bubbles moving in pseudo-orbits), the mean value of r_b is considered [25]. This change in r_b modifies the interaction between the acoustic emission of the bubble(s) and the normal modes of the acoustic resonator which in turn yields a change in the modulated components, i.e. the amplitude and relative phase of the observed harmonics. As a result, a causal mechanistic relation exist between modulating and modulated components in the AAC and APC patterns, which is represented as unidirectional arrows in the upper two rows of Table 1. The direction of this causal link is demonstrated in Section 4.4, where it is experimentally shown that the bubble radial position r_b does significantly affect the amplitude and relative phase of the intrinsic harmonics, but the opposite is not true.

It is essential to note that the PPC and PAC patterns (Figs. 9 and 10) emerge as a consequence of the AAC and APC couplings. That is, the amplitude of the fundamental frequency component (P_{LF}) effectively modulates the harmonics amplitude and relative phase. This modulation, in turn, leads to a correlation between the latter with the phase of the fundamental frequency component. Thus, the link between modulating and modulated parameters in the PAC and PPC patterns represents a correlation rather than a causal connection, which is represented by bidirectional arrows in the bottom two rows of Table 1.

4.4. Active manipulation of harmonics under SL conditions

The experiments described in this section were designed to study the direction of the causal link between modulating and modulated parameters regarding the APC and AAC couplings observed in the MIC signal (see Table 1). As discussed in Section 4.1, the presence of SL bubbles within the acoustic chamber is associated with the appearance of high-frequency harmonics ($\gtrsim 15f_0$) in the MIC signal [4,33] (see Fig. 2). This high-frequency harmonics are intrinsically produced by the interaction between the bubble(s) acoustic emission and the normal modes of the spherical resonator [19]. In line with this, bi-frequency driving was used to counteract an intrinsic high-frequency harmonic while monitoring the SL bubble dynamics (radial, spatial and positional). The bi-frequency driving was configured as follows. The amplitude of low-frequency driving (V_0) was tuned to trap a spatially stable (without pseudo-orbits) SL bubble near the center of the spherical resonator ($r_b < 10$ mm). Under this situation, the harmonic at $12f_0$, produced by the bubble-resonator interaction, was clearly identified in the spectrum of the MIC signal (see *Non-moving SBSL* case in Fig. 2). Then, the high-frequency driving V_{HF} was set at $12f_0$ ($\delta f = 0$) and the amplitude (V_{12}) and relative phase (α) were adjusted to minimize the amplitude of the spectral component at $12f_0$ present in the MIC signal. This fine tuning was implemented in real-time by processing the MIC with the FPGA-based lock-in system (see Fig. 1). After the tuning procedure, we alternated between single and bi-frequency driving following an ON/OFF protocol for V_{HF} in which the tuned parameters V_N, α, Nf_0 and δf were remained unchanged. Fig. 13 shows the bubble radial dynamics ($R(t)$) for both driving conditions(V_{HF} OFF and ON).

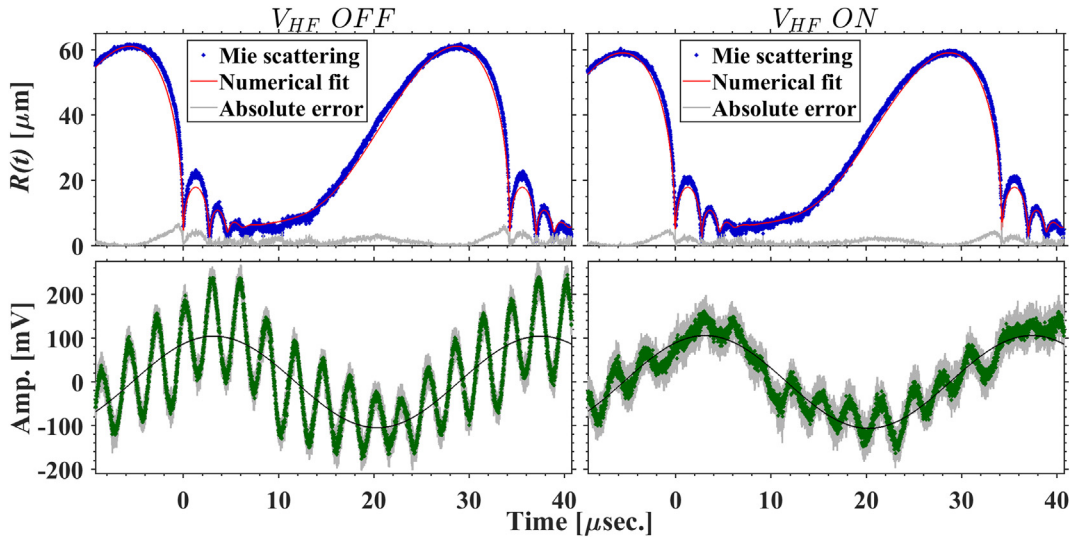

Fig. 13. Bubble radial dynamics and MIC signal under single and bi-frequency driving. (Upper graphs) Bubble radius temporal evolution $R(t)$ obtained from Mie scattering data for an argon SL bubble in SA85 (blue dots). The solid red curve represents the best numerical fit achieved (minimizing χ^2) using the RPK model and the light gray line is the absolute error. (Bottom graph) MIC signal showing the quasi-periodic non-sinusoidal waveform (green dots), superimposed to the fundamental frequency component (solid black line). The error bars are the standard deviation of 7 measurements at each point. For a dissolved argon concentration in SA85 of $c_\infty/c_{sat} \approx 0.006$, an spatially stable SL bubble was trapped at $r_b < 10$ mm using single frequency driving (Left graphs: V_{HF} OFF). Then, the high-frequency driving was turned on with V_{12} and α tuned to minimize the amplitude of the harmonic $12f_0$ observed in the MIC signal (Right graphs: V_{HF} ON). Fitted bubble parameters for V_{HF} OFF: $R_{max} = 61$ μm, $R_0 = 8.25 \pm 0.25$ μm, $P_{LF,b} = 1.66 \pm 0.04$ bar, $tc = 20.1 \pm 0.4$ μs. Fitted bubble parameters for V_{HF} ON: $R_{max} = 59$ μm, $R_0 = 8.25 \pm 0.08$ μm, $P_{LF,b} = 1.63 \pm 0.03$ bar, $tc = 19.9 \pm 0.4$ μs. The maximum absolute difference between the $R(t)$ of the bubble under V_{HF} ON and V_{HF} OFF driving conditions is 7% (computed from the Mie scattering data). (For interpretation of the references to colour in this figure legend, the reader is referred to the web version of this article.)

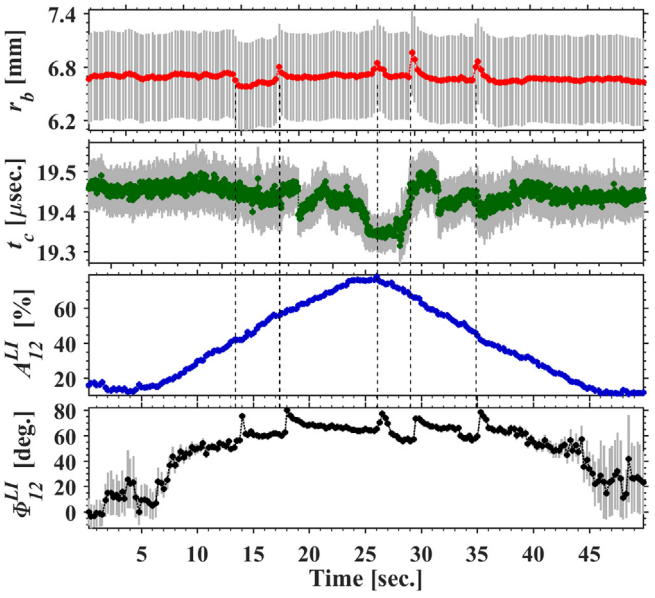

Fig. 14. Bi-frequency driving protocol implemented with a quasi-static ramp of V_{HF} amplitude, while monitoring the SL bubble radial position r_b and collapse time t_c. During this protocol, the amplitude (A_{12}^{LI}) and phase (Φ_{12}^{LI}) of the intrinsic harmonic $12f_0$ relative to the fundamental frequency component, were measured in real-time by means of processing the MIC signal with the lock-in system. For a dissolved argon concentration in SA85 of $c_\infty/c_{sat} \approx 0.006$, an spatially stable SL bubble was trapped at $r_b < 10$ mm using single frequency driving. Then, the high-frequency driving was turned on with V_{12} and α tuned to minimize the amplitude of the intrinsic harmonic $12f_0$ observed in the MIC signal ($\approx 15\%$ at $t < 5$ s). In the time interval $5\,\text{s} \leqslant t \leqslant 45\,\text{s}$, the driving amplitude V_{12} was gradually varied to produce ascending (up to $\approx 80\%$ at $t < 25$ s) and descending excursions of the intrinsic harmonic amplitude (A_{12}^{LI}). Vertical dashed lines indicates sporadic sudden changes of r_b, unrelated to the external driving, which produce significant changes in the phase Φ_{12}^{LI} corresponding to the component at $12f_0$ observed in the MIC signal.

During this experiment, the amplitude of the spectral component at $12f_0$ observed in the MIC signal relative to the amplitude of the fundamental frequency component (f_0), was reduced from 98% to 32% between the V_{HF} OFF and ON driving conditions respectively. In addition, quasi-static ramps of V_{HF} amplitude were also implemented keeping the α, Nf_0 and δf parameters unchanged. That is, the amplitude V_{12} was gradually increased/decreased with a rate of 3.3%/ s. corresponding to a change of 0.7% in a period of a pseudo-orbit (≈ 200 ms), with the latter being the largest time scale involved in the bubble dynamics (see insets (C)-(E) in Fig. 3). Using these protocols, the amplitude of the spectral component at $12f_0$ observed in the MIC signal was reduced from $\approx 80\%$ to $\approx 12\%$ while monitoring the SL bubble radial position r_b and collapse time t_c. Fig. 14 shows the system response to the implementation of a quasi-static ramp of V_{12}.

In order to explore the effects of changing the relative phase of the intrinsic harmonic $12f_0$, we also implemented some trials detuning V_{HF} by setting $\delta f = 0.7$ Hz. As a result, the amplitude and phase values obtained from the lock-in system corresponding to the channel referenced to $12f_0$ undergo oscillations at 0.7 Hz. Fig. 15 shows a typical result obtained switching δf from 0 to 0.7 Hz. During these bi-frequency experiments, no significant differences were observed between the bubble radial dynamics under the ON/OFF protocol for V_{HF}, either in the relative difference between the $R(t)$'s or in the bubble parameters R_{max}, R_0, $P_{LF,b}$ and tc (see the caption of Fig. 13). This result is consistent with previous reports about SL bubbles in water [30] and SA85 [26] systems. Moreover, during the quasi-static ramps of V_{HF} (Fig. 14) and the non-harmonic bi-frequency driving protocol (Fig. 15) the bubble radial position r_b exhibit fluctuations below the wavelength associated to the manipulated harmonic component ($\lambda = c_0/(12f_0) \approx 4$ mm for an speed of sound in the liquid of $c_0 = 1513$ m/s). In sum, it was found that the radial dynamics $R(t)$, spatial stability (pseudo-orbits) and radial bubble position r_b did not experience significant changes attributable to any of the bi-frequency protocols described above. This evidence suggest that the intrinsic harmonics produced by the bubble(s)-resonator interaction do not significantly affect the bubble dynamics.

Although sudden bubble displacements were observed during the

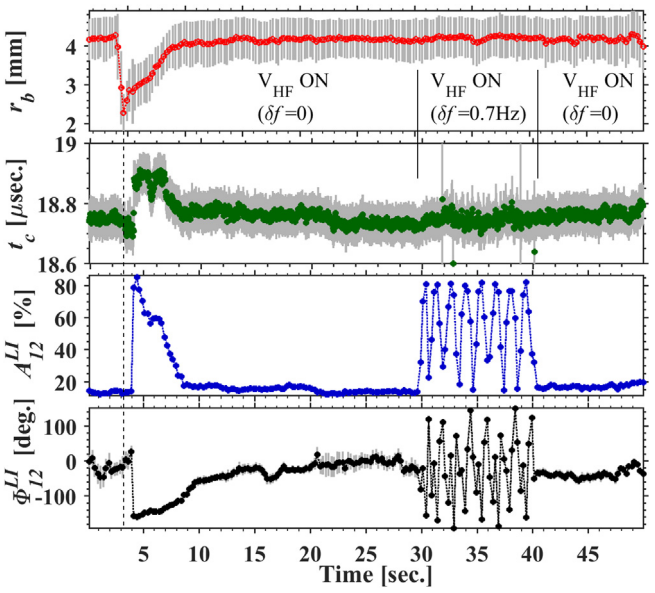

Fig. 15. Same experimental conditions as described in the caption of Fig. 14. In the time interval 30 s $\leqslant t \leqslant$ 40 s, the frequency of V_{HF} was varied by setting δf = 0.7 Hz. As a result, A_{12}^{LI} and Φ_{12}^{LI} measured by the lock-in system starts to oscillate at 0.7 Hz. The dashed vertical line indicates the time instant at the end of the shift of bubble radial position from $r_b \approx 4$ mm to $r_b \approx 2$ mm (unrelated to the external driving). Consistently, t_c increases since the bubble moves to a region of higher acoustic pressure, i.e. closer to the resonator center where the main pressure antinode is located. It is possible to appreciate a time lag between the shift of bubble radial position and the sudden changes observed in t_c, amplitude and phase of the harmonic.

bi-frequency experiments described above, their sporadic nature suggests that they were related to the complex acoustic environment of the SL bubble or impurities in the liquid rather than the action of external high-frequency driving. Importantly, Figs. 14 and 15 show that these sporadic sudden changes of r_b, unrelated to the external driving, produce significant changes in the relative amplitude and phase of the intrinsic harmonic component (see the dashed vertical lines in Figs. 14 and 15). In particular, the dashed vertical line in Fig. 15 indicates the time instant at the end of the shift of bubble radial position from $r_b \approx 4$ mm to $r_b \approx 2$ mm. Consistently, t_c increases since the bubble moves to a region of higher acoustic pressure, i.e. closer to the resonator center where the main pressure antinode is located. In Fig. 15 is possible to appreciate a time lag between the shift of bubble radial position and the sudden changes observed in t_c, amplitude and phase of the harmonic.

Taken together, these results show that the bubble radial position r_b does significantly affect the amplitude and relative phase of the intrinsic harmonics, but the opposite is not true. That is, a change in the bubble radial position modifies the interaction between the bubble acoustic emission with the normal modes of the acoustic resonator, which in turn yields a change in the amplitude and relative phase of the intrinsic harmonics. On the other hand, the amplitude of the intrinsic harmonics resulting from the bubble(s)-resonator interaction does not significantly affect the bubble dynamics (radial, spatial and positional). The direction of this causal link is represented by the unidirectional arrows corresponding to the upper two rows of Table 1.

It is worth noting that the spatial stability and the radial dynamics $R(t)$ of the SL bubble were only affected when external harmonic drivings V_{HF} ($3f_0 \leqslant Nf_0 \leqslant 12f_0$) were applied with amplitudes V_N much larger, at least 2 orders of magnitude, than those required to minimize the amplitude of intrinsic harmonics produced by the bubble(s)-resonator interaction [23]. As an example of the latter, Fig. 3 illustrates a spatially unstable SL bubble under single frequency driving (inset (F)) and the same SL bubble spatially stabilized (inset (G)) using a bi-harmonic driving with a large enough amplitude provided by the experimental setup of Fig. 1.

4.5. Advantages and sonochemical applications of the proposed techniques

It has been shown that the "epiphenomenal" PPC and PAC patterns can be exploited to determine the presence (Fig. 10), spatial stability (Figs. 5, 6 and 9) and radial position (Figs. 6, 8 and 12) of nonlinear oscillating bubble(s) trapped within the acoustic chamber. Moreover, it was experimentally demonstrated that the proposed methods, based on the quantification of CFC patterns, are robust enough to be used in a variety of acoustic scenarios: Single and Multiple nonlinear oscillating bubbles, spatially stable or instable (pseudo-orbits).

Detecting the presence of SL bubbles has been traditionally implemented using large bandwidths to monitor high-frequency harmonics ($\gtrsim 15f_0$) produced by the acoustic emission of the bubble, which are not masked by the nonlinear dynamics of the resonator (see Fig. 2) [4,33]. In Section 4.3, it was shown that the presence of nonlinear oscillating bubble(s) can be detected by monitoring the amplitude modulation depth of the PAC pattern (Fig. 10). Importantly, this technique can be implemented with a reduced bandwidth, about 1 order of magnitude ($\approx 3.5f_0$), compared to that required for the traditional methods ($\gtrsim 15f_0$).

A similar scenario was found for the bubble spatial stability, which is commonly obtained by monitoring the relative phase of the high-frequency oscillations ($\gtrsim 15f_0$) present in the MIC signal [1,21,32]. The results shown in Figs. 5, 6 and 9 suggest that the bubble(s) spatial stability can be inferred by monitoring the CFC patterns (e.g. dispersion of the PLV_N^{PPC} values) using a reduced bandwidth ($\gtrsim 2f_0$) compared to that required by previous techniques ($\gtrsim 15f_0$).

Due to the positional instability acting on argon and xenon SL bubbles in SA85, the bubble(s) radial position (r_b) could be directly obtained from the amplitude of low-frequency driving (V_0), or equivalently, by monitoring the fundamental frequency component of the acoustic pressure field (P_{LF}). However, the bubble radial position could be influenced by physical forces other than the hydrodynamic ones. For instance, one can imagine bubble(s)-resonator systems in which r_b is mainly determined by the dielectrophoretic force produced by an external electric field [34]. In such scenarios, r_b can no longer be obtained from V_0 or P_{LF}. It is remarkable that even in those cases, the "epiphenomenal" PPC and PAC patterns will still be informative about r_b, since they depend on the bubble(s)-resonator interaction irrespective of the physical forces acting on the bubble(s). In our acoustic system, it was found that the PPC and PAC patterns related to low-frequency harmonics ($\approx 2f_0$) can be used to estimate r_b (Figs. 6, 8 and 12). On the other hand, the PPC patterns related to high-frequency harmonics ($\approx 12f_0$) can be exploited to monitor the position of an spatially stable bubble relative to the location of pressure nodes corresponding to the high-frequency modes (Fig. 5).

The proposed techniques based on the quantification of CFC patterns from the MIC signal, are particularly useful to determine the presence, spatial stability and radial position of non-linear oscillating bubble(s) trapped within optically opaque resonators or liquids. For instance, they can be used in cavitation experiments aimed to explore the limits of the sonoluminescence phenomenon under high static pressures, which in general are implemented in resonators made of opaque materials (i.e. stainless steel) [35]. Moreover, such experiments can benefit from the proposed methods by using the bubble(s) radial position to perform a blind estimation of a) the acoustic pressure at the resonator center, provided the pressure profile of the excited acoustic mode is known and, b) the dynamics of the bubble(s), in cases where the concentration of dissolved gas in the liquid is known. That is, the Bjerknes force is responsible for the bubble(s) mean position and this imposes a limitation in the maximum acoustic pressure that can be applied to the bubble [18]. As a consequence, off-center bubble(s)

($r_b > 0$) lies just over the positional stability threshold. Therefore, the parameters associated to its dynamics can be obtained from the bubble parameters space $P_{LF,b}$–R_0 at the intersection between the Bjerknes threshold and the corresponding dissolved gas concentration contour [23,25].

Taking into account that non-radially symmetric vibration modes of the spherical resonator can be also excited under SL bubble scenarios, CFC patterns associated to the polar or azimuthal spherical coordinates of the SL bubble position would be also possible. In this regard the feasibility of three-dimensional estimation of the bubble position, based on CFC patterns processing from a single or multi acoustic sensors, has to be demonstrated.

5. Conclusions

In this work it was found that, in absence of bubbles, the acoustic chamber is capable to oscillate in a nonlinear regime characterized by inter-mode couplings where acoustic energy is drained from the resonator first mode by the high-frequency modes. The resulting non-sinusoidal dynamics was constituted by harmonics ranging from $f_0 \approx$ 29.15 kHz to $15 f_0 \approx$ 450 kHz. It was shown that this harmonic content produced "spurious" cross-frequency couplings (CFC). On the other hand, the bubble(s)-resonator interaction in the oscillatory steady-state was characterized by non-sinusoidal waveforms constituted by harmonics ranging from $f_0 \approx$ 29.15 kHz to above $35 f_0 \approx$ 1 MHz. As a consequence of the bubble(s)-resonator mechanistic interaction, "causal" amplitude-to-amplitude (AAC) and amplitude-to-phase (APC) cross-frequency couplings were present in the MIC signal.

We have shown that the presence, spatial stability and the radial position of the bubble(s) can be estimated from the MIC signal by quantifying the "epiphenomenal" phase-to-phase (PPC) and phase-to-amplitude (PAC) couplings, which emerges as a consequence of the "causal" AAP and APC patterns. This novel technique is suitable to be used in presence of external forces acting on the bubble(s) other than the hydrodynamic ones. Due to the fact that the proposed methods are based only on the measurement of acoustic signals, they result particularly relevant in applications involving optically opaque resonant chambers or liquids.

Substantial evidence was presented showing that CFC patterns emerging from quasi-periodic non-sinusoidal waveforms are informative on the interaction between underlying oscillators.

Acknowledgements

This work was partially supported by ANPCyT (PICT 2014-1966) and UNCuyo SeCTyP (05/C016), Argentina. J.M.R. was supported with a postdoctoral scholarship granted by CONICET. The authors gratefully appreciate the support of Fabián Bonetto in providing access to the L.C.B. facilities.

Appendix A. Electronics and instrumentation

A tailored multifrequency electronics for concurrent signal synthesis and measurement based on Field Programmable Gate Array (FPGA) technology was developed to perform the experiments described in this work [21,27]. This custom instrumentation was arranged in the experimental setup shown in Fig. 1, specialized for characterizing the nonlinear harmonics present in the acoustic field and its active manipulation in real-time as described in Section 4. In Fig. 1, the FPGA board provide, through a 12 bits D/A converter (*Linear Technology DAC LTC2624*) with a sample rate of $f_s \gtrsim 10\ f_0$, a low-distortion sinusoidal signal tuned to the resonance of the acoustic chamber first mode ($f_0 \approx$ 29.15 kHz). In order to prevent introducing high-frequency artifact spuriously induced by the digital electronics, the driving signal is conditioned in amplitude (*LF Amp.* in Fig. 1) and then bandpass (BP) filtered (quality factor $Q \approx 10$) by a low-noise preamplifier *Stanford Research Systems Model SR650*. After that, the signal was amplified by a power audio amplifier (*Radioshack* 100 W, $V_{out}|_{max} =$ 70 Vrms) which feeds a RLC_{PZT} circuit ($Q \approx 15$), tuned via the inductance L to maximize the voltage signal applied to the *PZT* drivers ($V_{LF}|_{max} \approx$ 1000 Vrms). It is worth noting that, an additional BP filtering of the driving signal V_{LF} occurs due to the narrow full-width half-power bandwidth $Bw_0 = f_0/Q \approx$ 117 Hz of the acoustic resonator first mode (measured $Q \approx$ 250) [19,21].

The response of the acoustic resonator was obtained using the electrical signal provided by the MIC. The stop-band effect of the high-pass filter formed by the intrinsic piezo-capacitance of the MIC connected in series with the input impedance of the amplifier, was mitigated using high-input impedance amplifiers. Accordingly, we couple the MIC to the low-noise preamplifier and configurable BP filter *Stanford Research Systems Model SR560* (input impedance $100M\Omega//25pF$) and a custom made amplifier with input impedance greater than 1 MΩ (*Amp. 1* in Fig. 1). The *SR560* was configured as an anti-aliasing filter with a pass-band of 10 kHz–1 MHz. Then, the MIC signal was acquired by a *GW-Instek Model 2204* oscilloscope at a sampling rate of 2.5 Msps and a memory depth of 25 k samples (*Oscilloscope 1* in Fig. 1) [22].

Alternatively, the amplified version of the MIC signal at the output of *Amp. 1* in Fig. 1, was digitized by and A/D converter (channel 1 of *Linear Technology ADC LTC1407A-1*, 14 bits, 1.5 Msps) to be processed in real-time by the lock-in system implemented in the FPGA board, which is capable of measuring up to 5 frequencies simultaneously at ≈ 4 sps with an equivalent noise bandwith $ENBW \approx$ 40 Hz. The amplitudes and phases of the harmonics and the fundamental frequency constituting the MIC signal are measured in real-time with respect to the internal reference of the digital lock-in and stored in a standard computer (*PC3* in Fig. 1). During the experiments, the collapse time of the bubble (t_c) was measured by a timer *Stanford Research Systems SR620*. The timer start event was given by the zero crossing with negative slope of the fundamental component (f_0) of the MIC signal. Besides, the SL pulse was detected using an *Oriel 77340* phototube which provides the stop signal to the timer. The timer was operated at its maximum sampling rate (≈ 1500 t_c values/s) with a precision of 100 ns (determined by the jitter in the MIC signal). The measured t_c values were stored in a computer (*PC1* in Fig. 1). The radial coordinate (r_b) of the SL bubble inside the spherical chamber was determined from the images provided by a CCD camera (*Hitachi KPF120*) arranged perpendicularly to the bubble trajectory. The camera also registers the measurement displayed by the *HP 34401A* voltmeter. It is important to remark that, the fundamental component (f_0) of the MIC signal is stored in *PC3* via A/D channel 0 of the FPGA board, and in *PC1*, through the *Oscilloscope 2* (see Fig. 1). This allows to perform the synchronization of the measurements stored in both computers, during the posterior processing of the data. On the other hand, the amplitude of the low-frequency driving V_{LF} was simultaneously registered by the *Oscilloscope 2* and the *Hitachi KPF120* camera which allows for the posterior synchronization of the data stored in *PC1* and *PC2*. During the experiments using bi-harmonic driving of the acoustic chamber, the high-frequency signal (V_{HF}) provided by the custom-made D/A ΔΣ converter (effective number of bits *ENOB*= 6 bits at *Bw*= 500 kHz) was amplified using a custom-built low distortion high-voltage amplifier (*HV Amp.*, *Bw*= 400 kHz at C_L= 2 nF) to excite the high-frequency drivers (PZT_{HF}) [21].

Appendix B. Computation of the analytic signal and band-pass filter configurations

We computed the analytic signal $x^+(n)$ in the frequency domain using the following equations [29],

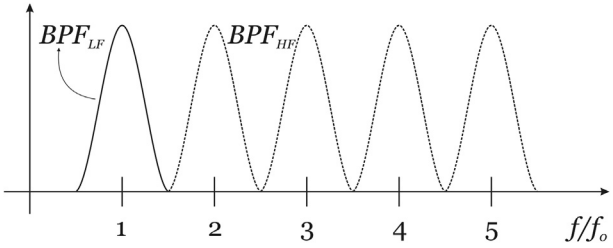

Fig. B.16. Band-pass filter configuration for phase-to-phase coupling (PPC). The BPF_{LF} filter is centered at $f_{LF}^{c} = f_0$ with a bandwidth of $Bw = f_0$. The BPF_{HF} filters are centered at $f_{HF}^{c} = Nf_0$ with a bandwidth of $Bw = f_0$.

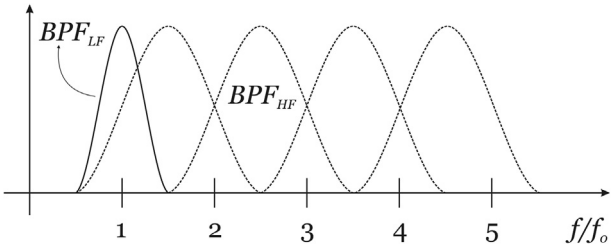

Fig. B.17. Band-pass filter configuration for phase-to-amplitude coupling (PAC). The BPF_{LF} filter is centered at $f_{LF}^{c} = f_0$ with a bandwidth of $Bw = f_0$. The BPF_{HF} filters are centered at $f_{HF}^{c} = (N + 0.5)f_0$ with a bandwidth of $Bw = 2f_0$.

$$
\begin{aligned}
&X(f) = FFT\{x(n)\}\\
&X^{+}(f) = \begin{cases} 2X(f), & \forall f > 0 \\ X(0), & \forall f = 0 \\ 0, & \forall f < 0 \end{cases}\\
&x^{+}(n) = iFFT\{X^{+}(f)\},
\end{aligned}
\tag{B.1}
$$

where $FFT\{.\}$ and $iFFT\{.\}$ denote the Fourier Transform and its inverse respectively, computed via the Fast Fourier Transform algorithm.

Figs. B.16 and B.17 illustrate the band-pass filter configurations used to process the MIC signal in order to quantifying the CFC patterns of type phase-to-phase coupling (PPC) and phase-to-amplitude coupling (PAC).

In the case of the band-pass filter configuration for PAC and considering a MIC signal $x_{MIC}(n)$ constituted by the sum of harmonic sinusoids, the analytic signal $x_{HF}^{+}(n)$ corresponding to the output of the BPF_{HF} centered at $f_{HF}^{c} = (N + 0.5)f_0$ can be written as follows,

$$x_{HF}(n) = A_N \cos(\omega_N n) + A_{N+1} \cos((\omega_N + \omega_0)n + \Phi_{N+1}) \tag{B.2}$$

$$
\begin{aligned}
&\omega_N = N\omega_0\\
&\hat{x}_{HF}(n) = A_N \sin(\omega_N n) + A_{N+1} \sin((\omega_N + \omega_0)n + \Phi_{N+1})
\end{aligned}
\tag{B.3}
$$

$$
\begin{aligned}
x_{HF}^{+}(n) &= x_{HF}(n) + j\hat{x}_{HF}(n)\\
&= A_N e^{j(\omega_N n)} + A_{N+1} e^{j(\omega_N n)} e^{j(\omega_0 n)} e^{j\Phi_{N+1}}
\end{aligned}
\tag{B.4}
$$

From Eq. (B.4) we obtain that the amplitude envelope $a_{HF}(n)$ of $x_{HF}(n)$ signal depends on the harmonics amplitude (A_N, A_{N+1}) besides its relative phase (Φ_{N+1}). In the particular case of harmonic components with identical amplitude we obtain,

$$
\begin{aligned}
&A_N = A_{N+1} = A\\
&a_{HF}(n) = |x_{HF}^{+}(n)| = \left|2A \cos\left(\frac{\omega_0 n + \Phi_{N+1}}{2}\right)\right|
\end{aligned}
\tag{B.5}
$$

References

[1] D. Dellavale, J.M. Rosselló, Cross-frequency coupling and phase synchronization in nonlinear acoustics, in: Proceedings of Meetings on Acoustics (Acoust. Soc. Am.), vol. 28, 2016, 055001.https://doi.org/10.1121/2.0000294.

[2] G.F. Puente, Sonoluminiscencia y cavitación en burbujas: Análisis dinámico y de estabilidad en regiones altamente no lineales (Ph.D. thesis), Instituto Balseiro, 2005;
G.F. Puente, R. Urteaga, F.J. Bonetto, Numerical and experimental study of dissociation in an air-water single-bubble sonoluminescence system, Phys. Rev. E 72 (2005) 046305;
G.F. Puente, P. García-Martínez, F.J. Bonetto, Single-bubble sonoluminescence in sulfuric acid and water: bubble dynamics, stability, and continuous spectra, Phys. Rev. E 75 (2007) 016314, https://doi.org/10.1103/PhysRevE.75.016314.

[3] D.F. Gaitan, A. Crum, C. Church, A. Roy, Sonoluminescence and bubble dynamics for a single, stable, cavitation bubble, J. Acoust. Soc. Am. 91 (6) (1992) 3166, https://doi.org/10.1121/1.402855.

[4] F.B. Seeley, Effects of higher-order modes and harmonics in single-bubble sonoluminescence, J. Acoust. Soc. Am. 105 (4) (1999) 2236–2242, https://doi.org/10.1121/1.426828.

[5] K. Johnston, et al., Periodic shock-emission from acoustically driven cavitation clouds: a source of the subharmonic signal, Ultrasonics 54 (8) (2014) 2151–2158, https://doi.org/10.1016/j.ultras.2014.06.011.

[6] B.J. He, et al., The temporal structures and functional significance of scale-free brain activity, Neuron 66 (3) (2010) 353–369, https://doi.org/10.1016/j.neuron.2010.04.020.

[7] A.C. Onslow, R. Bogacz, M.W. Jones, Quantifying phase-amplitude coupling in neuronal network oscillations, Prog. Biophys. Mol. Biol. 105 (1–2) (2011) 49–57, https://doi.org/10.1016/j.pbiomolbio.2010.09.007.

[8] J. Aru, et al., Untangling cross-frequency coupling in neuroscience, Curr. Opin. Neurobiol. 31 (2015) 51–61, https://doi.org/10.1016/j.conb.2014.08.002.

[9] S.R. Cole, B. Voytek, Brain oscillations and the importance of waveform shape, Trends Cogn. Sci. 21 (2) (2017) 137–149, https://doi.org/10.1016/j.tics.2016.12.008.

[10] A.C. Onslow, et al., A canonical circuit for generating phase-amplitude coupling,

PLoS One 9 (8) (2014) e102591, https://doi.org/10.1371/journal.pone.0102591.
[11] D. Lozano-Soldevilla, et al., Neuronal oscillations with non-sinusoidal morphology produce spurious phase-to-amplitude coupling and directionality, Front. Comput. Neurosci. 10 (2016) 87, https://doi.org/10.3389/fncom.2016.00087.
[12] P. Tass, et al., Detection of n:m phase locking from noisy data: application to magnetoencephalography, Phys. Rev. Lett. 81 (1998) 3291, https://doi.org/10.1103/PhysRevLett. 81.3291.
[13] W.D. Penny, et al., Testing for nested oscillation, J. Neurosci. Methods 174 (1) (2008) 50–61, https://doi.org/10.1016/j.jneumeth.2008.06.035.
[14] M.X. Cohen, Assessing transient cross-frequency coupling in EEG data, J. Neurosci. Methods 168 (2) (2008) 494–499, https://doi.org/10.1016/j.jneumeth.2007.10.012.
[15] A.B. Tort, et al., Measuring phase-amplitude coupling between neuronal oscillations of different frequencies, J. Neurophysiol. 104 (2) (2010) 1195–1210, https://doi.org/10.1152/jn.00106.2010.
[16] M.X. Cohen, Analyzing Neural Time Series Data, Theory and Practice, The MIT Press, 2014.
[17] J.I. Berman, et al., Variable bandwidth filtering for improved sensitivity of cross-frequency coupling metrics, Brain Connect. 2 (3) (2012) 155–163, https://doi.org/10.1089/brain.2012.0085.
[18] R. Urteaga, D.H. Dellavale, G.F. Puente, F.J. Bonetto, Positional stability as the light emission limit in sonoluminescence with sulfuric acid, Phys. Rev. E 76 (2007) 056317, https://doi.org/10.1103/PhysRevE.76.056317.
[19] D. Dellavale, R. Urteaga, F. Bonetto, Analytical study of the acoustic field in a spherical resonator for single bubble sonoluminescence, J. Acoust. Soc. Am. 127 (1) (2010) 186–197, https://doi.org/10.1121/1.3257208.
[20] R. Urteaga, Concentración de energía en sonoluminiscencia (Ph.D. thesis), Instituto Balseiro, 2008.
[21] D. Dellavale, Algoritmos para el procesamiento concurrente de señales y su aplicación en sonoluminiscencia (Ph.D. thesis), Instituto Balseiro, 2011.
[22] J.M. Rosselló, Frontera de estabilidad en sonoluminiscencia y concentración de energía en cavitación transitoria forzada (Ph.D. thesis), Instituto Balseiro, 2015.
[23] D. Dellavale, L. Rechiman, J.M. Rosselló, F. Bonetto, Upscaling energy concentration in multifrequency single-bubble sonoluminescence with strongly degassed sulfuric acid, Phys. Rev. E 86 (2012) 016320.
[24] L.M. Rechiman, D. Dellavale, F.J. Bonetto, Path suppression of strongly collapsing bubbles at finite and low Reynolds numbers, Phys. Rev. E 87 (2013) 063004.
[25] J.M. Rosselló, D. Dellavale, F.J. Bonetto, Stable tridimensional bubble clusters in multi-bubble sonoluminescence (MBSL), Ultrason. Sonochem. 22 (2015) 59–69.
[26] J.M. Rossell, D. Dellavale, F.J. Bonetto, Positional stability and radial dynamics of sonoluminescent bubbles under bi-harmonic driving: effect of the high-frequency component and its relative phase, Ultrason. Sonochem. 31 (2016) 610–625, https://doi.org/10.1016/j.ultsonch.2016.02.013.
[27] D. Dellavale, et al., FPGA based Multi-Harmonic Control System for Single Bubble Sonoluminescence, in: 4th Southern Conference on Programmable Logic, IEEE, Piscataway, NJ, 2008, p. 269.https://doi.org/10.1109/SPL.2008.4547774.
[28] R.G. Holt, L.A. Crum, MIE scattering used to determine spherical bubble oscillations, Appl. Opt. 29 (1990) 4182, https://doi.org/10.1364/AO.29.004182.
[29] Simon Haykin, Communication Systems, fouth ed., John Wiley & Sons, 2000.
[30] Joachim Holzfuss, Matthias Rggeberg, R. Glynn Holt, Acoustical stability of a sonoluminescing bubble, Phys. Rev. E 66 (2002) 046630, https://doi.org/10.1103/PhysRevE.66.046630.
[31] P.M. Morse, K. Uno Ingard, Theoretical Acoustics, McGraw-Hill, 1970.
[32] Jaroslav Plocek, A method for indication and improving the position stability of the bubble in single-bubble cavitation experiments, Rev. Sci. Instrum. 88 (2017) 104901, https://doi.org/10.1063/1.5006100.
[33] Shigeo Hayashi, et al., Acoustic emission from a sonoluminescing bubble, Acoust. Sci. Technol. 22 (2001) 2.
[34] S.J. Shaw, et al., Electrically induced bubble deformation, translation and collapse, J. Eng. Math. 65 (4) (2009) 291–310, https://doi.org/10.1007/s10665-009-9314-y.
[35] D.F. Gaitan, et al., Transient cavitation in high-quality-factor resonators at high static pressures, J. Acoust. Soc. Am. 127 (2010) 3456–3465, https://doi.org/10.1121/1.3377062.